ICJK
Journal of Advanced Materials Research
http://dx.doi.org/10.62762/JAMR.2026.894537

RESEARCH ARTICLE

A Dynamic Core Modulation Strategy for Enhancing Active Sites of Polymer-Derived Carbon Electrocatalysts

Zidan Zhang[1,†], Huan Wu[1,†], Boyu Jia[1], Qingmin Ji[1,*] and Hengdao Quan[2]

[1] Herbert Gleiter Institute of Nanoscience, School of Materials Science and Engineering, Nanjing University of Science and Technology, Nanjing 210094, China
[2] School of Materials and Chemistry, University of Shanghai for Science and Technology, Shanghai 200093, China

Abstract

Polymer-derived carbons have emerged as efficient and economical electrocatalysts for energy-related reactions such as oxygen reduction and hydrogen evolution. However, their performance often faces an inherent trade-off between porosity and electronic conductivity, necessitating precise regulation of composition and structure at the molecular level. To enhance the formation of accessible active sites, we construct a series of core@polyaniline precursors with systematically varied organic cores (a nitrogen-rich polymer (NPS), polysaccharide (GluS), and polyaniline (PANI) itself). Metals ions are introduced during the shell polymerization. The resultant core-shell precursors were then subjected to pyrolysis, where the carbon network forms with Fe-N active sites generated inside. We propose that the core polymer remotely modulates the formation of active sites in the carbon shell during pyrolysis. Through combined structural characterization and electrocatalytic evaluation, we find that the nitrogen-rich polymeric core, which undergoes pronounced volume change during pyrolysis, promotes the formation of a more graphitized, electron-conductive carbon network with a higher density of accessible Fe-N sites. In contrast, the polysaccharide core with a mild pyrolysis profile and the chemically identical PANI core lack this dynamic templating ability and do not effectively optimize the carbon structure. Through this dynamic core modulation, a Fe/Ni co-loaded catalyst was also prepared, achieving excellent bifunctional ORR/HER performance, with an ORR half-wave potential of 0.89 V (vs RHE) and an HER overpotential of 298 mV, along with good stability. This work provides a new perspective for the rational design of polymer-derived carbon electrocatalysts, shifting attention from static precursor composition to the dynamic role of the core during pyrolysis.

Keywords: polymer-derived carbons, metal-N active sites, core-shell polymers, electrocatalysis, core-to-shell remote modulation.

Submitted: 29 May 2026
Accepted: 27 June 2026
Published: 06 July 2026

Vol. 2, **No.** 3, 2026.
10.62762/JAMR.2026.894537

***Corresponding author:**
✉ Qingmin Ji
jiqingmin@njust.edu.cn

† These authors contributed equally to this work

Citation
Zhang, Z., Wu, H., Jia, B., Ji, Q., & Quan, H. (2026). A Dynamic Core Modulation Strategy for Enhancing Active Sites of Polymer-Derived Carbon Electrocatalysts. *Journal of Advanced Materials Research*, 2(3), 169–194.

1 Introduction

Polymer-derived carbon materials have emerged as a prominent class of functional carbon materials with wide applications in energy-related electrochemical devices, owing to their molecular-level tunability and structural designability [1]. This tunability allows for tailored incorporation of heteroatoms and metal active sites into the carbon framework, which may enhance the catalytic activity. Especially, conductive polymers, such as polyaniline (PANI) and polypyrrole (PPy), have received extensive attention as nitrogen-rich carbon precursors [2, 3]. However, the strong interchain hydrogen bonding or rigid conjugated backbones in these polymers may induce compact stacking during pyrolysis, leaving a large fraction of potential active sites buried within the matrix and inaccessible to reactants. Achieving a favorable balance between active site density and active site accessibility has thus been a persistent challenge.

To overcome this structural limitation, core-shell structured polymer precursors have been widely adopted as a design platform [4, 5]. In principle, core-shell structured catalysts have been extensively reviewed across thermocatalytic, photocatalytic, and electrocatalytic systems, where the core component serves distinct structural roles in directing the architecture and active site distribution of the resulting catalyst [6]. For example, Nguyen et al. [7] used polystyrene (PS) spheres as a sacrificial core and coated them with a polypyrrole and bimetallic ZIF shell to fabricate a Fe, Co, and N co-doped carbon electrocatalyst. The complete decomposition of the PS core during pyrolysis left behind a hollow carbon shell with enhanced porosity and active site accessibility. Jiao et al. [8] employed a MOF as the core and a rigid porous organic polymer as the shell, which prevented pore collapse during pyrolysis and facilitated nitrogen doping through a post-impregnation step. The resulting catalyst achieved a high concentration of active sites and a hierarchical pore architecture, delivering ORR activity and stability superior to commercial Pt/C. In both cases, the core is essentially treated as a static entity that provides space or mechanical support. However, different polymers can exhibit markedly different pyrolysis behaviors. A core undergoing dramatic volumetric change is unlikely to be merely a passive spectator. The mechanical stress and chemical gradients generated at the core-shell interface should, in principle, influence the carbonization pathway of the shell and the distribution of active sites. This possibility motivates a reconsideration of the role of the core during structural evolution. Whether the dynamic physical evolution of the core can be harnessed to modulate the structural and catalytic properties of the shell remains an open question.

To understand the dynamic influence of the core, herein, we designed three types of core-shell polymeric structures by using PANI as the shell and different organic cores, which are a nitrogen-rich spherical core known to undergo pronounced volume change during pyrolysis, a polysaccharide-derived core with a mild and gradual pyrolysis profile, and a chemically identical PANI core that eliminates any core-shell compositional difference (Figure 1). Fe ions were introduced during the shell polymerization step, ensuring that active site precursors are uniformly distributed within the shell. Based on a combination of structural characterization, thermogravimetric analysis, and electrocatalytic evaluation, it was found that the nitrogen-rich polymeric core produces the optimal carbon network in the shell with the highest density of accessible metal-N active sites. Since the shell composition and metal loading protocol are the same for the three polymer systems, it suggests that the core rather than acting solely as a passive template, can remotely direct the formation of the carbon network and active sites in the shell via its pyrolysis-induced physical evolution. Building on this "core-to-shell remote modulation" concept, we further demonstrate the generality of the strategy by extending it to bimetallic Fe/Ni systems, achieving competitive bifunctional ORR/HER performance. This work provides a new perspective for the rational design of polymer-derived carbon electrocatalysts, shifting attention from the static chemistry of carbon precursors to the dynamic physical processes that may also govern active site formation during pyrolysis.

2 Experimental section

2.1 Materials

Aniline (C_6H_7N, ≥99.9%) was purchased from Rhawn (Shanghai) Chemical Technology Co., Ltd. Anhydrous ethanol (C_2H_6O, AR) was purchased from Sinopharm Chemical Reagent Co., Ltd (Shanghai, China). Ammonium persulfate ($(NH_4)_2S_2O_8$, 99.99%) was purchased from Aladdin Reagent Co., Ltd (Shanghai, China). Iron(III) chloride hexahydrate ($FeCl_3{\cdot}6H_2O$, AR, 99%) was purchased from Aladdin Reagent Co., Ltd. Glucose ($C_6H_{12}O_6$, AR) was purchased from Aladdin Reagent Co., Ltd. Urea (CH_4N_2O, AR, 99%) was purchased from Aladdin Reagent Co., Ltd.

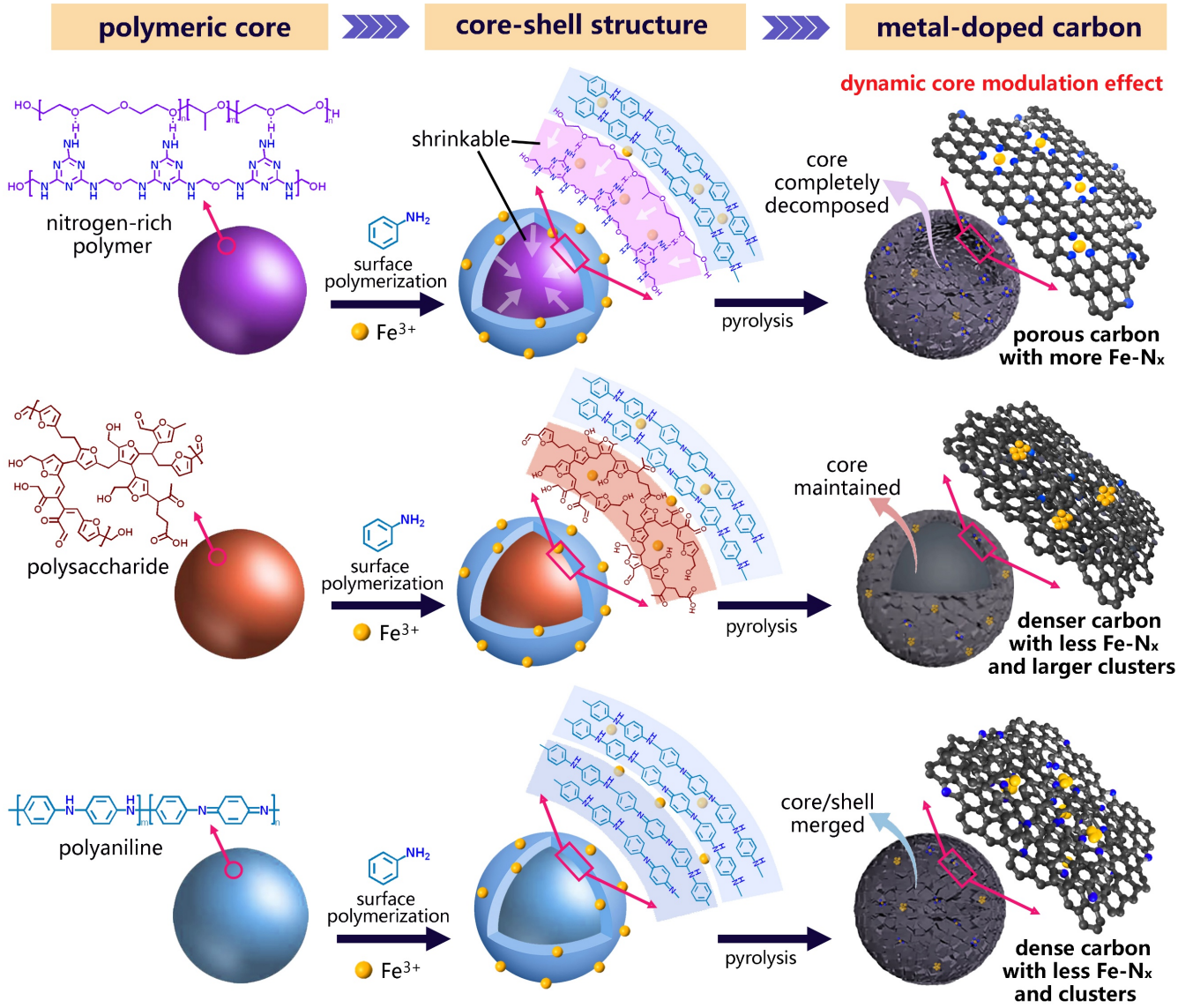

Figure 1. Schematic of metal-doped carbon electrocatalysts derived from diverse core-shell polymeric structures. Optimization of the carbon network to expose accessible active sites via the dynamic core modulation effect.

Pluronic F-127 (polyoxyethylene-polyoxypropylene block copolymer) was purchased from Sigma-Aldrich. Mesitylene (C_9H_{12}, 98%) was purchased from Energy Chemical (Shanghai, China). Melamine ($C_3H_6N_6$, 99%) was purchased from Aladdin Reagent Co., Ltd. Formaldehyde (CH_2O, 37% 40%) was purchased from Adamas-beta (Shanghai, China). Sodium hydroxide (NaOH, AR) was purchased from Sinopharm Chemical Reagent Co., Ltd. Hydrochloric acid (HCl, AR) was purchased from Sinopharm Chemical Reagent Co., Ltd. Nickel chloride ($NiCl_2$, 99%) was purchased from Macklin (Shanghai) Biochemical Technology Co., Ltd. The Pt/C catalyst was purchased from Suzhou Sinero Technology Co., Ltd. All chemicals were used as received without further purification.

2.2 Preparation of organic cores

(1) **Nitrogen-rich polymer spheres (NPS).** A solution A was prepared by dissolving 0.6 g of Pluronic F-127 in 10 mL of deionized water, and mixing 0.6 g of mesitylene (TMB) under stirring for 6 h. Separately, solution B was prepared by mixing 3 mmol of melamine, 3 mmol of formaldehyde aqueous solution (37 wt%), and 50 μL of NaOH solution (0.1 M) in 40 mL of deionized water under stirring at 100 °C for 30 min. Solution A was then added to solution B and stirred for an additional 2 h. Subsequently, 0.81 mmol of HCl was introduced, and the mixture was stirred continuously for 12 h. The resulting product was collected by centrifugation and washed three times each with deionized water and anhydrous ethanol.

(2) **Polysaccharide spheres (GluS).** 1.4 g of glucose and 0.45 g of urea were dissolved in 21 mL of an ethanol–water solution (2:1, v/v). After stirring for 30 min, the resulting mixture was transferred into a Teflon-lined autoclave and heated at 180 °C for 10 h. The precipitate was collected by centrifugation and washed four times with deionized water.

(3) **Polyaniline particles (PANI).** 2 mmol of aniline was dissolved in 5 mL of ethanol and cooled to −5 °C in an ice bath. 60 mL of deionized water was then added. After 30 min, 35 mL of a pre-cooled saturated ammonium persulfate (APS) solution was introduced, and the reaction was allowed to proceed for 12 h. The product was collected by centrifugation at 6000 rpm and washed four times with deionized water.

2.3 Preparation of core-shell structure

Washed NPS, GluS and PANI (core polymers) were dispersed in 60 mL of an aqueous solution containing 6.25 mmol/L $FeCl_3$ or a mixed solution of 6.25 mmol/L $FeCl_3$ and 6.25 mmol/L $NiCl_2$. A dispersion of aniline (2 mmol) in 5 mL of ethanol was added dropwise under vigorous stirring. The reaction mixture was then cooled to −5 °C in an ice bath and maintained at this temperature for 30 min to ensure uniform adsorption of aniline monomers onto the particle surfaces. Thereafter, 35 mL of pre-cooled saturated APS aqueous solution was slowly introduced to initiate polymerization. The reaction was allowed to proceed for 12 h under static conditions at −5 °C. The resulting core-shell composites were collected by centrifugation at 6000 rpm, followed by repeated washing with deionized water (four times) to remove residual reactants and byproducts. The products were finally freeze-dried under vacuum.

2.4 Carbonization of the metal-loaded core-shell polymers

The dried Fe- or Fe/Ni-loaded core-shell polymers (e.g. NPS@PANI, GluS@PANI, and PANI@PANI) were subjected to controlled pyrolysis under nitrogen atmosphere. The samples were heated from room temperature to 900 °C at a heating rate of 5 °C·min^{-1} and held at this temperature for 2 h to ensure complete carbonization. The resulting materials were denoted as N@P-Fe, G@P-Fe, P@P-Fe, and N@P-FeNi, corresponding to the original precursors and their metal loadings (Fe-only or Fe/Ni bimetallic).

2.5 Characterizations

Scanning electron microscopy (SEM) images were acquired using a Zeiss Sigma 360 field emission scanning electron microscope operating at 10 kV. Transmission electron microscopy (TEM) was operated on a JEM-F200 at a voltage of 200 kV. X-ray diffraction (XRD) patterns were collected on a Bruker D8 Advance diffractometer with Cu K_α radiation ($\lambda = 1.5406$ Å). Nitrogen sorption isotherms were measured at 77 K using a Micromeritics Gemini VII 2390 surface area and porosity analyzer. Specific surface areas were calculated based on the Brunauer-Emmett-Teller (BET) method. Thermogravimetric-differential scanning calorimetry (TG-DSC) analyses were carried out on a NETZSCH STA 409 PC Jupiter instrument under a nitrogen atmosphere, with a heating rate of 10.0 °C·min^{-1} from 30 to 900 °C. X-ray photoelectron spectroscopy (XPS) measurements were conducted on a Thermo Scientific K-Alpha spectrometer using Al K_α radiation (hv = 1486.6 eV). Raman spectra were recorded on a Horiba LabRAM Aramis confocal Raman spectrometer equipped with a 514 nm Ar^+ ion laser operating at a power of 10 mW.

2.6 Electrochemical measurement

The oxygen reduction reaction (ORR) and hydrogen evolution reaction (HER) activities of the catalysts were evaluated in a standard three-electrode electrochemical cell using KOH as the electrolyte. ORR measurements were conducted in O_2-saturated 0.1 M KOH, and HER measurements in 1 M KOH, following the standard protocols adopted in literature [9, 10]. A catalyst-modified glassy carbon electrode (GCE, 5 mm in diameter), a Hg/HgO (1 M KOH) reference electrode, and a graphite rod served as the working, reference, and counter electrodes, respectively.

The working electrode was prepared by ultrasonically dispersing 5 mg of catalyst in 1 mL of methanol for 1 h to form a homogeneous ink. Subsequently, 15 μL of the ink was drop-cast onto a mirror-polished GCE surface, resulting in a catalyst loading of 0.38 mg cm^{-2}. After drying at ambient temperature, the electrode was coated with 5 μL of a 0.1 wt% Nafion ethanol solution and dried again to form a protective film.

The electrochemical surface area (ECSA) was estimated by measuring the double-layer capacitance (C_{dl}) in the non-Faradaic potential region of 1.05–1.15 V vs. RHE at scan rates of 10–70 mV·s^{-1}. The charging current density ($\Delta i = (i_{\text{anodic}} - i_{\text{cathodic}})/2$) at the

center potential was plotted against scan rate, and C_{dl} was determined from the slope of the linear fit. The ECSA was then calculated using the equation:

$$\mathrm{ECSA} = \frac{C_{dl}}{C_s} \tag{1}$$

where C_s is the specific capacitance of a smooth electrode (typically 0.040 mF·cm^{-2} for carbon-based materials in alkaline media).

Cyclic voltammetry (CV) measurements were carried out in N_2- or O_2-saturated 0.1 M KOH at a scan rate of 50 mV·s^{-1} over a potential window of 0.0–1.2 V versus the reversible hydrogen electrode (RHE). All potentials recorded against the Hg/HgO reference were converted to the RHE scale using the equation:

$$E(\text{vs. RHE}) = E(\text{vs. Hg/HgO}) + 0.098\ \text{V} + 0.059 \times \text{pH} \tag{2}$$

Linear sweep voltammetry (LSV) for ORR was performed in O_2-saturated 0.1 M KOH at a scan rate of 10 mV·s^{-1} with electrode rotation rates ranging from 400 to 2500 rpm. Rotating ring-disk electrode (RRDE) measurements were conducted under identical conditions with the ring potential held at 1.4 V vs. RHE to detect peroxide intermediates. The electron transfer number (n) and H_2O_2 yield (%) were calculated from the disk and ring currents using the following equations:

$$n = \frac{4I_D}{I_D + I_R/N} \tag{3}$$

$$\mathrm{H_2O_2\%} = \frac{200 \times (I_R/N)}{(I_D + I_R/N)} \tag{4}$$

where I_D and I_R are the disk and ring currents, respectively, and N is the ring collection efficiency ($N = 0.37$, as determined by experimental calibration using the $[Fe(CN)_6]^{3-}/[Fe(CN)_6]^{4-}$ redox couple).

3 Results and Discussion

3.1 Structure and pyrolysis behavior of core-shell polymeric composites

Three types of organic core with distinct molecular structures were first synthesized individually. NPS was prepared via acid-catalyzed polycondensation of melamine and formaldehyde, using Pluronic F-127 as a soft template and mesitylene as a pore-swelling agent, following a reported procedure for melamine resin-based porous carbons [11]. GluS was synthesized by hydrothermal carbonization of glucose and urea at 180 °C following a reported hydrothermal procedure [12], producing a carbonaceous skeleton rich in oxygen-containing functional groups. PANI was obtained by oxidative polymerization of aniline with ammonium persulfate as the oxidant, adapting a protocol established for aniline-derived iron–nitrogen–carbon electrocatalyst preparation [13]. Its backbone comprises alternating phenyl and quinoid rings linked by amine ($-$NH$-$) and imine ($-$N $=$) groups, forming a rigid and fully conjugated chain. These three cores represent chemically distinct nitrogen/oxygen environments, which may isolate the effect of core chemistry on subsequent carbonization.

The SEM images revealed that the NPS were uniform spheres with diameters of 200–300 nm, the GluS showed a similar spherical morphology with larger diameters of 400–500 nm, and PANI appeared as irregular agglomerates of small particles (Figure 3(a-c)). Thermogravimetric analysis (TGA) under an inert atmosphere revealed pronounced differences in their pyrolysis behavior (Figure 2(a-c)). NPS exhibited a major weight loss between 300 and 400 °C, followed by a gradual decrease that approached near-zero residual mass at 900 °C. This early-stage rapid decomposition indicates extensive fragmentation and volatilization of the melamine-formaldehyde network [14]. By contrast, GluS and PANI displayed a more gradual weight loss starting from approximately 200 °C and retained roughly 50% of their initial mass at 900 °C. The substantial difference in char yield suggests that NPS undergoes a far more dramatic physical transformation during carbonization than the other two cores.

The morphological changes after heat treatment at 500 °C were further confirmed by SEM (Figure 3(d-f)). This intermediate temperature was selected based on TGA results, which showed that the NPS core undergoes major decomposition between 300–400 °C. At 500 °C, it has substantially decomposed while still partially retaining its structural framework. As shown in Figure 3(d), NPS remained spherical but shrank to roughly half of their original diameter. GluS retained their spherical morphology with negligible size change, while PANI particles fused into dense, irregular blocks, losing their original granular texture. X-ray diffraction (XRD) patterns of the carbonized cores displayed a broad peak around 25°, which is characteristic of the (002) interlayer diffraction

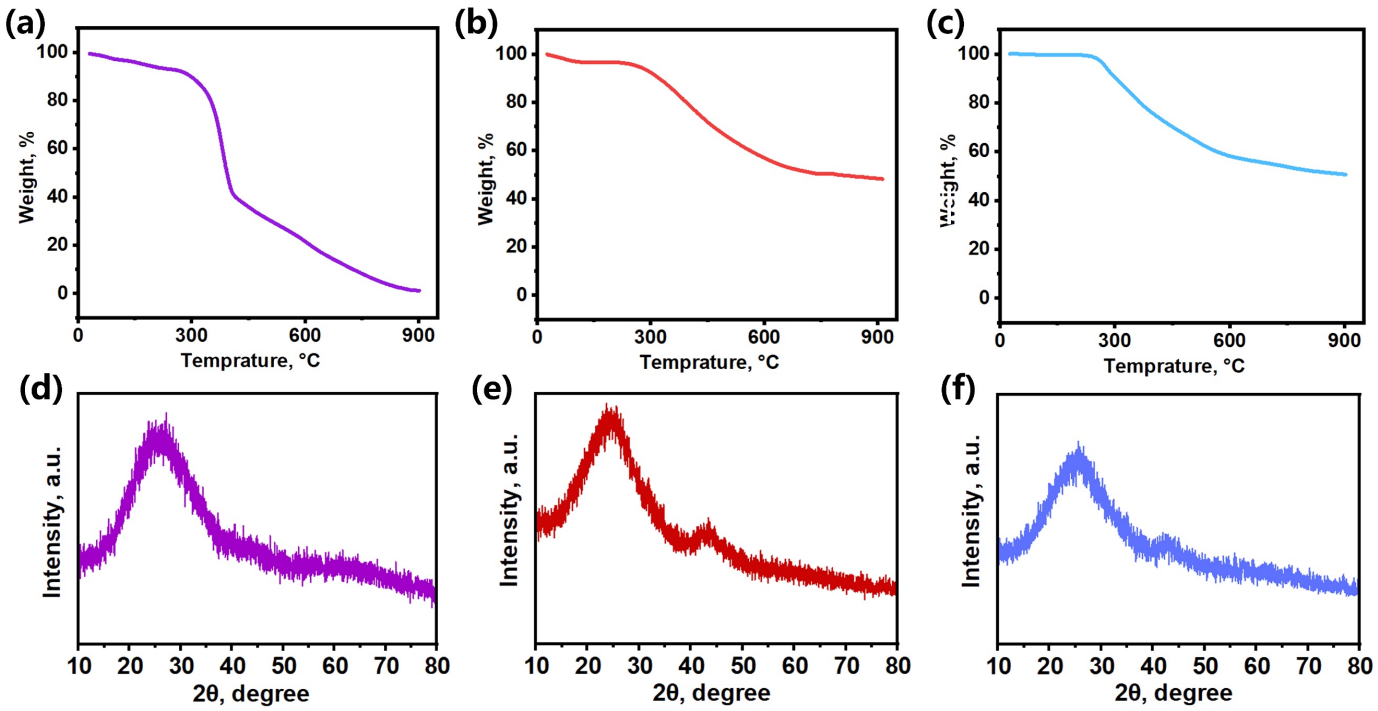

Figure 2. TGA curves of (a) NPS, (b) GluS, and (c) PANI under N_2 atmosphere. XRD patterns of (d) NPS, (e) GluS, and (f) PANI after annealing.

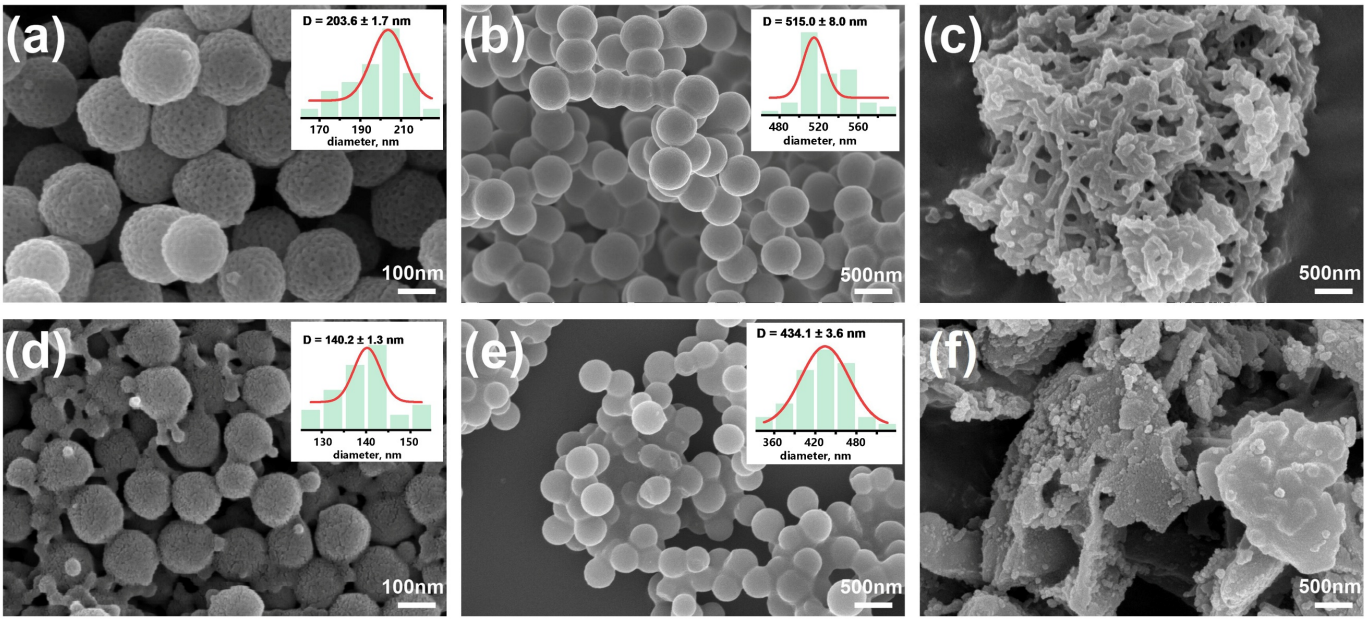

Figure 3. SEM images of (a-c) as-synthesized NPS, GluS, and PANI, and (d-f) the corresponding samples after annealing at 500 °C. The inset are particle size distributions of NPS and GluS from statistical analysis of >30 spheres from SEM images.

of disordered graphitic carbon (Figure 2(d-f)). However, GluS and PANI further exhibited a weak, broad diffraction peak at approximately 40–50°, attributable to the (100)/(101) in-plane diffraction of graphitic carbon, a feature commonly observed in heteroatom-doped carbon electrocatalysts with partial in-plane structural ordering [15]. The presence of this signal suggests that the GluS- and PANI-derived carbons possess a modest degree of in-plane structural ordering within their carbon layers, whereas such a feature is absent for NPS. These results establish a clear hierarchy of pyrolysis behavior among the three cores. NPS undergoes violent decomposition with massive volume loss. By contrast, GluS exhibits mild pyrolysis

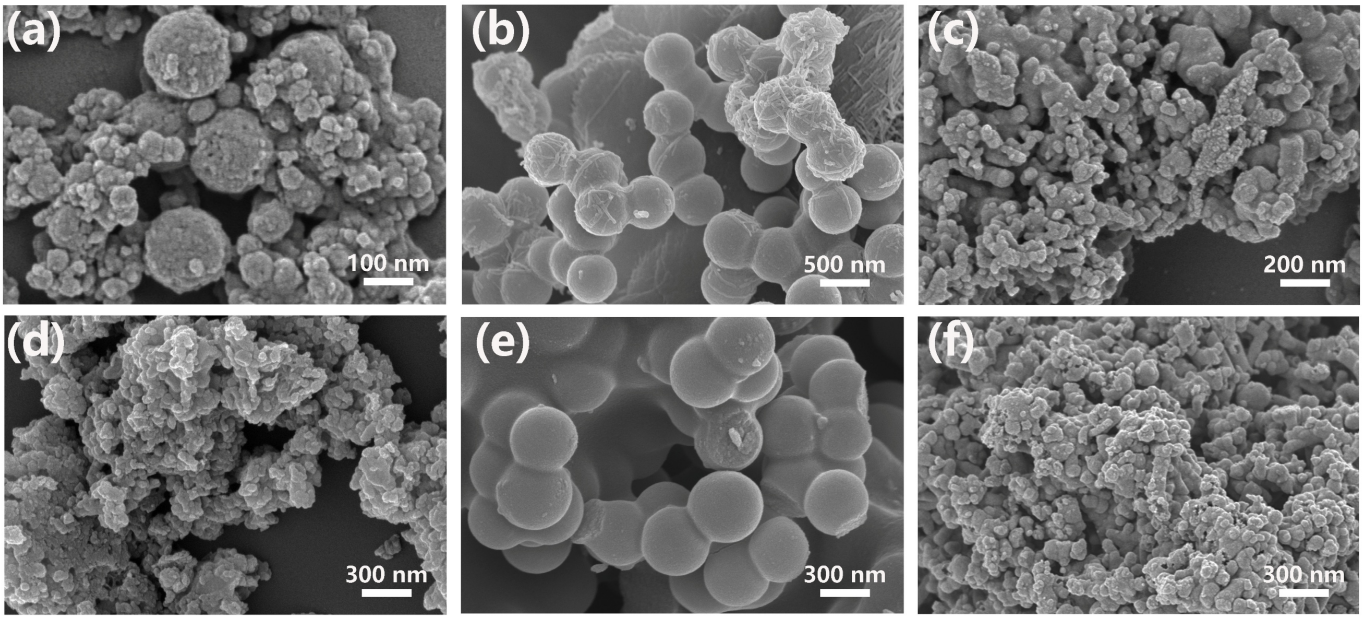

Figure 4. SEM images of core-shell precursors before pyrolysis, (a) NPS@PANI, (b) GluS@PANI, and (c) PANI@PANI. SEM images of the Fe-doped carbons derived from core-shell precursors with Fe^{3+} after pyrolysis, (d) N@P-Fe, (e) G@P-Fe and (f) P@P-Fe.

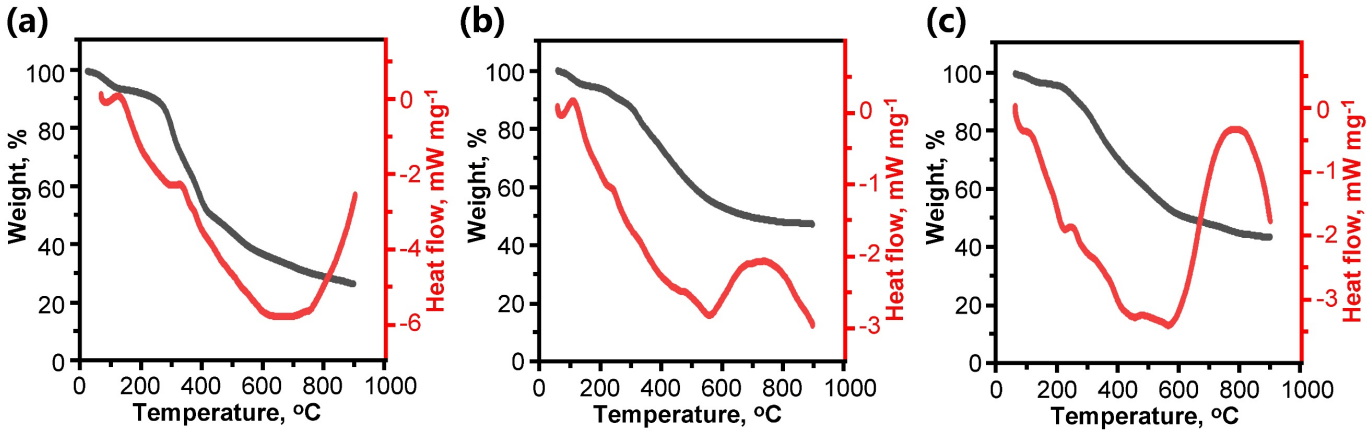

Figure 5. TGA/DSC profiles of (a) NPS@PANI, (b) GluS@PANI, and (c) PANI@PANI under N_2 atmosphere from room temperature to 900 °C.

with strong structural persistence, while PANI is morphologically unstable but thermally similar to GluS.

Each as-prepared core was subsequently coated with a PANI shell by in-situ polymerization of aniline on the surfaces. The resultant core-shell composites are denoted as NPS@PANI, GluS@PANI, and PANI@PANI. SEM images of the composite particles showed a roughened surface texture with small granular features, indicative of PANI deposition on the core surface (Figure 4(a-c)). TG-DSC analysis of the core-shell precursors revealed that the presence of the PANI shell significantly modulated the thermal behavior compared to the bare cores (Figure 5). All three samples displayed a weak endothermic peak around 100 °C, which is attributed to the evaporation of residual water within the structures. NPS@PANI showed a distinct DSC exothermic peak at approximately 300 °C. Since this peak was absent in the DSC profiles of the other two core-shell systems, it can be assigned to the confined decomposition of the NPS core beneath the PANI shell. In contrast, PANI@PANI exhibited another small exothermic peak centered at around 220 °C, consistent with the thermally induced structural transitions of polyaniline previously reported across various composite systems [16]. The absence of this PANI-characteristic peak in both NPS@PANI and GluS@PANI suggests that the intrinsic structural rearrangements of PANI are suppressed or altered by the presence of a chemically distinct core.

GluS@PANI, by contrast, displayed no discernible exothermic events below 500 °C, consistent with the mild and gradual pyrolysis profile of the GluS core itself.

At higher temperatures, all three systems underwent a pronounced thermal transition corresponding to carbonization, but they followed different pathways. PANI@PANI exhibited the most pronounced high-temperature features. Its DSC profile displayed a plateau beginning at approximately 400 °C, followed by a sharp endothermic rise starting at around 580 °C. A well-defined endothermic peak, which is the most prominent among the three systems, appeared at approximately 800 °C. This intense endothermic event can be attributed to the extensive structural decomposition and volatilization of the PANI phase [17]. Since the core and shell of PANI@PANI are chemically identical, this concentrated endothermic peak suggests that the entire structure undergoes extensive bond cleavage and heteroatom removal as a single phase.

By comparison, the DSC curve of GluS@PANI was decreased steadily until approximately 550 °C, at which point it began an immediate shift toward the endothermic direction until up to around 710 °C without an intervening plateau. This result suggests that the oxygen-rich GluS core may catalyze or alter the early stages of shell carbonization, initiating the endothermic decomposition at a lower temperature. NPS@PANI displayed the most delayed and protracted high-temperature behavior. Its DSC profile began a gradual change at around 600 °C, then entered a plateau region before finally exhibiting a steady endothermic rise from approximately 700 °C. Unlike the other two systems, this rise continued up to 900 °C without reaching a turning point. This suggests that the carbonization of the PANI shell in NPS@PANI is fundamentally altered. Considering the dramatic volume changes of NPS and near-complete mass loss observed for the NPS core upon heating, it is plausible that the core develops a partially hollow interior during the early stages of pyrolysis. Such a loss of a rigid core support may lead to a more gradual and less cooperative structural evolution of the PANI-derived carbon shell, stretching the decomposition process over a wider temperature range.

To enhance the catalytic activity of the core-shell composite-derived carbons, metal ions were introduced during the formation of the PANI shell. The nitrogen and oxygen functionalities present in both the core and shell structures can serve as coordination sites for metal ions; such N- and O-containing environments in carbonaceous matrices have been shown to anchor a broad range of transition metal species, including those formed via coordination during polymer precursor processing [18, 19]. Compared with their metal-free counterparts, the Fe-loaded core-shell composites exhibited reduced particle uniformity, with more small particulate debris surrounding the spheres (Figure S1). As Fe^{3+} ions can serve as an additional oxidant or co-initiator alongside APS during aniline polymerization, it thus could alter the nucleation and growth kinetics of the PANI shell, leading to a less uniform coating compared with the metal-free counterparts.

The presence of Fe ions also influenced the morphology of the core-shell composites after pyrolysis at 900 °C (Figure 4(d-e)). For clarity, the carbonized samples are denoted as N@P-Fe, G@P-Fe, and P@P-Fe, corresponding to the Fe-loaded NPS@PANI, GluS@PANI, and PANI@PANI, respectively. N@P-Fe completely lost its original spherical morphology, transforming into an irregular, aggregated carbon structure with no vestige of the core-shell template. TEM elemental mapping of N@P-Fe revealed a uniform distribution of C, N, and Fe throughout the carbon matrix (Figure S2). In contrast, G@P-Fe preserved well-defined spheres with smooth surfaces. This confirms that the GluS core could provide persistent structural support throughout carbonization. P@P-Fe retained its particulate character but became denser with tightly packed aggregates, suggesting enhanced carbonization-induced shrinkage.

It should be noted that neither N@P-Fe nor G@P-Fe exhibited a hollow spherical morphology or a distinct core-shell interface after carbonization. To clarify whether the core and shell components are structurally distinguishable, control experiments were conducted using a sequential synthesis protocol, in which Fe was pre-loaded onto the core before PANI shell polymerization. After carbonization, the NPS-based precursor yielded a hollow spherical structure, confirming complete decomposition of the NPS core and retention of the PANI-derived carbon shell (Figure S3). The GluS-based precursor displayed a core-shell morphology with a dark-contrast central region (Fe-rich GluS-derived carbon) surrounded by a lighter PANI-derived carbon layer (Figure S4). These results confirm that the two polymer components can

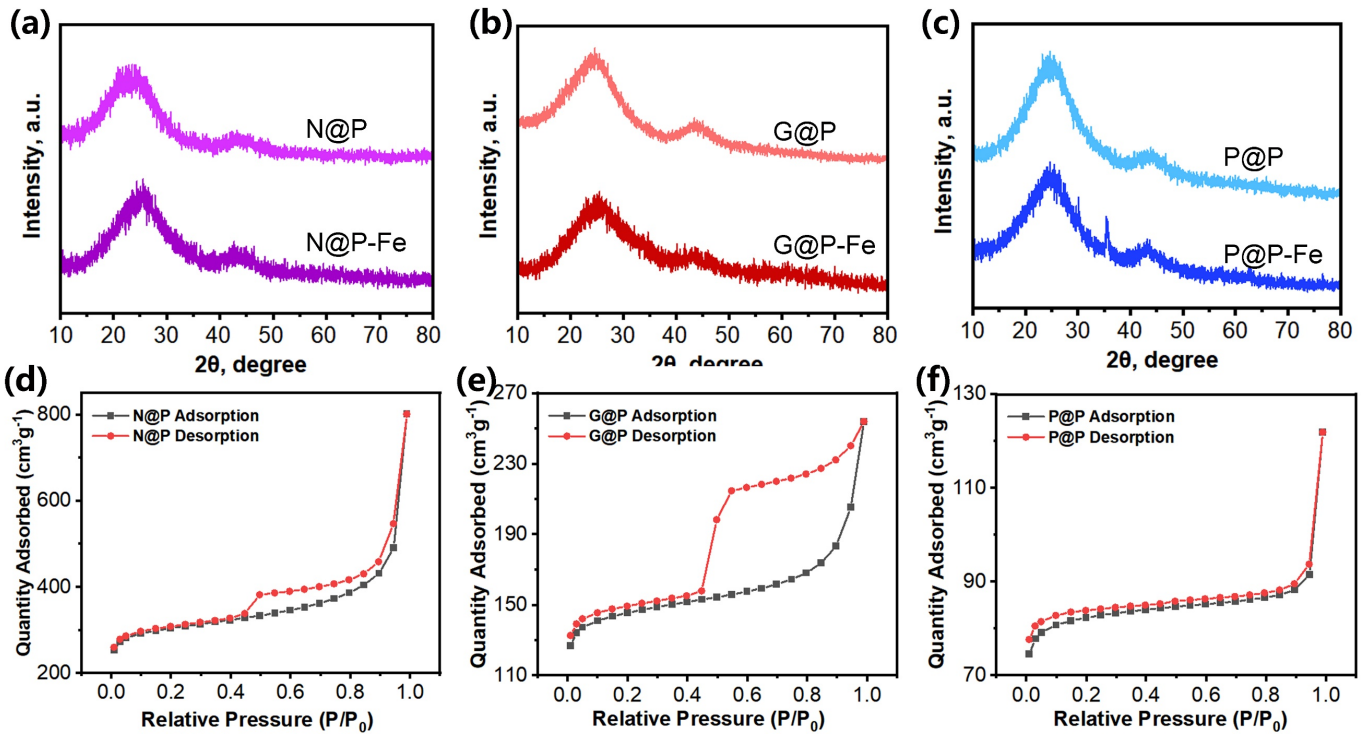

Figure 6. (a-c) XRD patterns of the derived carbons from core-shell precursors pyrolyzed without Fe doping (N@P, G@P, P@P) and with Fe doping (N@P–Fe, G@P-Fe, P@P-Fe). N_2 sorption isotherms of (d) N@P, (e) G@P and (f) P@P.

be assembled into a core-shell configuration. The absence of a visible interface in N@P-Fe and G@P-Fe is therefore attributed to the case when Fe^{3+} and aniline are introduced together during PANI shell polymerization (the simultaneous Fe introduction protocol).

This structural difference arises from the distinct roles of Fe^{3+} in the two protocols. When introduced simultaneously with aniline, Fe^{3+} coordinates with both the core surface functionalities and the amine/imine groups of PANI chains, acting as an interfacial crosslinker that promotes network interpenetration and eventual interface fusion upon carbonization. When pre-loaded onto the core, Fe^{3+} remains anchored at the core surface without bridging the two phases. This intimate interfacial contact achieved in the simultaneous protocol is expected to maximize the remote modulation of the core on shell carbonization.

3.2 Comparison of carbon network structures and active site configuration

The core-dependent influence on the carbon network structure and metal dispersion in the core-shell-derived carbons was further examined by XRD, N_2 sorption, Raman, and XPS analyses.

XRD patterns of the Fe loaded carbonized samples were collected to assess both the carbon framework structure and the dispersion state of iron species (Figure 6(a-c)). For N@P-Fe and G@P-Fe, the broad (002) peak shifted slightly toward higher diffraction angles relative to their metal-free counterparts (N@P and G@P). This shift reflects a decrease in the carbon interlayer spacing, pointing to a more compact and partially ordered carbon framework. Moreover, no additional diffraction peaks corresponding to crystalline Fe phases were detected in either sample, suggesting that Fe is highly dispersed in the form of atomically distributed state or sub-nanometer clusters below the detection limit of XRD. Unlike N@P-Fe and G@P-Fe, the (002) peak position in diffraction pattern of P@P-Fe remained unchanged compared with metal-free P@P. In addition, P@P-Fe exhibited sharp diffraction peaks at 31° and 36°, which can be assigned to crystalline Fe-containing phases, such as Fe_3C or iron oxides [20, 21]. These signals imply the formation of larger and aggregated Fe species rather than atomic-level dispersion.

To assess the porosity and surface area of the core-shell-derived carbons, N_2 sorption measurements were performed on the core-shell derived carbons (Figure 6(d-e)). The three core-shell systems displayed Type IV isotherms characteristic of mesoporous materials with different hysteresis behaviors. N@P exhibited a distinct hysteresis loop

in the relative pressure (P/P_0) range of 0.4–0.9, indicating the presence of well-developed mesopores. The sharp increase in N_2 uptake above $P/P_0 = 0.9$ can be attributed to the filling of large mesopores or inter-particle macropores. G@P displayed a much broader and more pronounced hysteresis loop in the P/P_0 of 0.4–0.9, suggesting a more extensive and continuous mesopore network. In contrast, P@P showed a nearly featureless isotherm with negligible hysteresis, consistent with a poorly porous, densely packed carbon structure.

The BET specific surface areas followed the order of N@P (963 $m^2 \cdot g^{-1}$) > G@P (463 $m^2 \cdot g^{-1}$) > P@P (255 $m^2 \cdot g^{-1}$) (Table S1). Notably, the total pore volume of N@P (0.35 $cm^3 \cdot g^{-1}$) was approximately twice that of G@P (0.18 $cm^3 \cdot g^{-1}$) and more than three times that of P@P (0.11 $cm^3 \cdot g^{-1}$). This pronounced difference in pore volume highlights the critical role of the NPS core in generating a porous, accessible carbon architecture.

To further probe the influence of Fe loading on Fe dispersion and carbon structure evolution, the Fe content in the N@P system was systematically varied (Figure S5). At the lowest Fe loading (N@P-Fe1, Fe:aniline = 1:16), the (002) peak was shifted toward lower diffraction angles compared with intermediate Fe loading (N@P-Fe2, 1:6). A more obvious appearance of the broad peak at approximately 42°, suggested enhanced in-plane ordering and the onset of incipient graphitization in N@P-Fe2. For the highest Fe loading (N@P-Fe3, 1:4), the (002) peak intensity markedly decreased, reflecting a disruption of the compact framework. Simultaneously, multiple sharp diffraction peaks appeared at approximately 32°, 36°, 57°, and 65°. These peaks can be attributed to crystalline Fe species, indicating the formation of metal aggregation under excessive Fe loading.

Raman spectroscopy was employed to probe the degree of structural ordering in the carbon networks (Figure 7). All samples displayed the characteristic D band (~1350 cm^{-1}) and G band (~1580 cm^{-1}) of carbon materials, corresponding to the defect-induced breathing mode of sp^2 rings and the in-plane bond-stretching vibration of sp^2 carbon, respectively [22]. The metal-free samples revealed pronounced core-dependent differences in the initial carbon network quality. N@P exhibited a notably shallow valley between the D and G bands, indicative of a substantial contribution from amorphous carbon and a highly disordered carbon framework. G@P displayed a more pronounced D-G valley, suggesting a comparatively lower fraction of amorphous carbon. These results are consistent with the XRD and TGA results discussed above, where the near-complete decomposition of the NPS core may leave behind a highly disrupted carbon residue, whereas the GluS core could retain an ordered framework.

To quantify these spectral changes, the Raman spectra were deconvoluted into the G band and three additional sub-bands of D^4 (~1180 cm^{-1}), D^1 (~1350 cm^{-1}), and D^3 (~1510 cm^{-1}), corresponding to sp^2-sp^3 mixed carbon, disordered graphitic domains, and amorphous carbon [23], respectively (Figure 7). The intensity ratio of the D^3 band to the G band (I_{D3}/I_G) served as a semi-quantitative indicator of the amorphous carbon fraction. Among the metal-free samples, N@P exhibited the highest I_{D3}/I_G ratio (0.589), indicating the highest fraction of amorphous carbon, consistent with the near-complete decomposition of the NPS core during pyrolysis (Table S2). Upon Fe loading, N@P-Fe showed a significant reduction in I_{D3}/I_G to 0.499, suggesting that Fe promotes the conversion of amorphous carbon into a more graphitized structure. In contrast, G@P-Fe and P@P-Fe exhibited only marginal changes in I_{D3}/I_G compared with their metal-free counterparts (Table S2). These results suggest that the combination of the dynamic NPS core and Fe loading synergistically promotes the conversion of disordered carbon into a more graphitized, less defective framework.

X-ray photoelectron spectroscopy (XPS) was employed to investigate the surface chemical states and elemental composition of the core-shell-derived carbons (Figure S6). For the metal-free samples, N@P exhibited the highest total nitrogen and oxygen contents among the three systems (Table S3). Deconvolution of the N 1s spectra revealed four nitrogen species, which are pyridinic N (~398.5 eV), pyrrolic N (~399.8 eV), graphitic N (~401.0 eV), and oxidized N (~402.5 eV) (Figure 8(a-c)). N@P contained the highest fraction of pyridinic nitrogen (Table S4), which is widely recognized as the primary coordination site for anchoring Fe ions to form active Fe–N_x moieties [24]. G@P displayed a higher proportion of pyrrolic and oxidized nitrogen, while P@P was dominated by graphitic nitrogen. The C 1s spectra further corroborated these trends (Figure S7). N@P exhibited the highest C–N component among the three samples (Table S5), indicating that a larger fraction of nitrogen was covalently incorporated into the carbon framework. The C–C/C=C component dominated the C 1s spectra of all samples, consistent

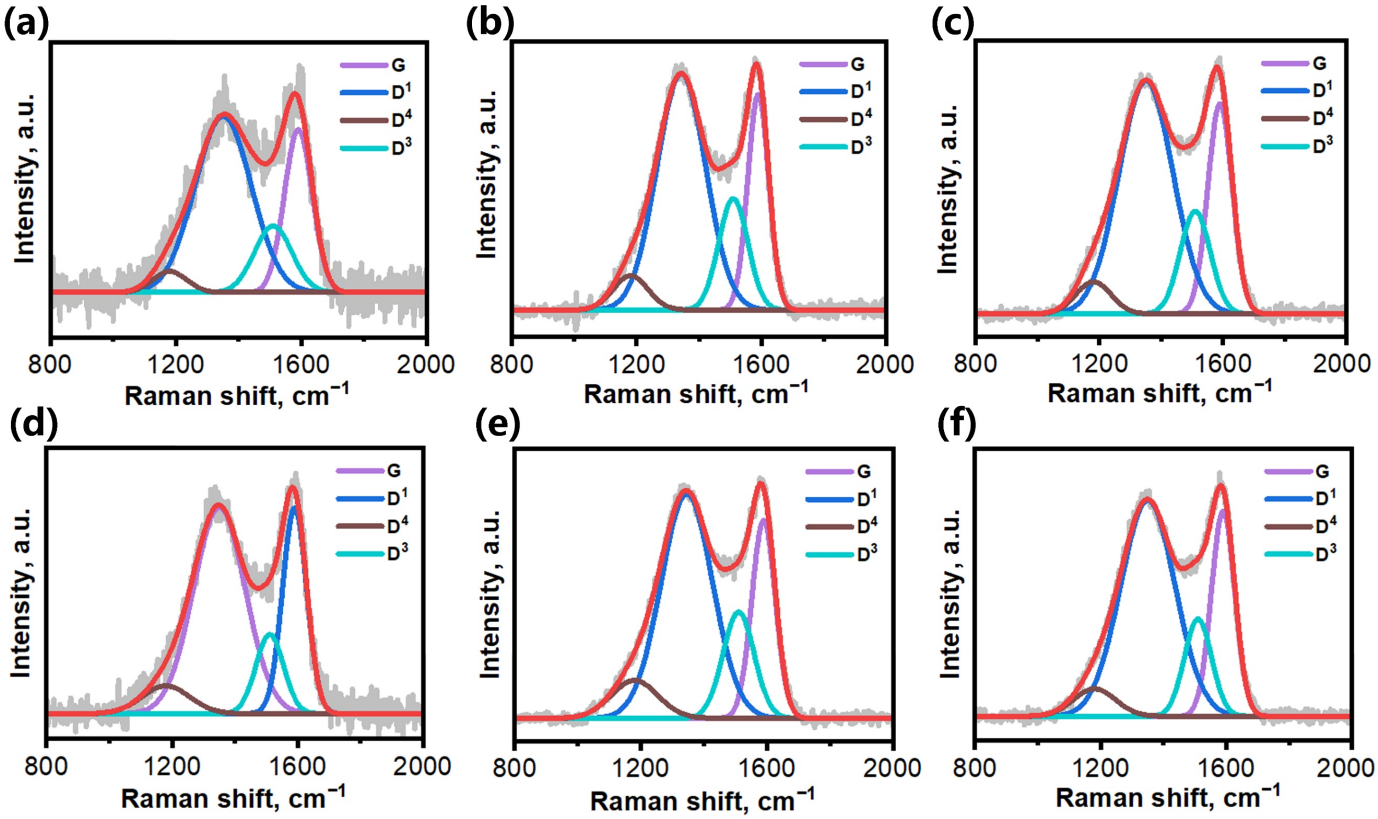

Figure 7. Raman patterns of the derived carbons from core-shell precursors pyrolyzed without Fe doping (a) N@P, (b) G@P, (c) P@P), and with Fe doping (d) N@P–Fe, (e) G@P-Fe, (f) P@P-Fe).

with their carbon nature.

Upon Fe loading, the total Fe content based on XPS analysis, followed the order P@P-Fe > N@P-Fe > G@P-Fe (Table S3). The Fe 2p spectra were deconvoluted into Fe^{2+} (~708.5 eV), Fe^{3+} (~710.5 eV), and Fe^0 (~706.8 eV) components (Figure 8(d-f)). N@P-Fe possessed the highest proportion of Fe^{2+}, the characteristic oxidation state of Fe in Fe–N_x active sites [25]. Despite having the highest total Fe content, P@P-Fe exhibited a lower Fe^{2+} fraction, consistent with the XRD evidence of crystalline iron carbide/oxide formation (Table S6). G@P-Fe was dominated by Fe^{3+} and Fe^0 signals, suggesting the presence of oxidized iron nanoparticles or metallic Fe aggregates. The N@P system was further examined by varying the Fe loading (Figure S8, Table S6). Among the three Fe loadings investigated, N@P-Fe2 (Fe:aniline = 1:6) exhibited the highest fraction of both Fe–N species and pyridinic nitrogen in the N 1s spectrum. Combined with the XRD results, this suggests that N@P-Fe2 represents an optimal Fe loading for maximizing the formation of atomically dispersed Fe–N_x sites in the structure.

To further explore the generality of the core-to-shell modulation strategy, a bimetallic FeNi-loaded N@P catalysts (N@P-FeNi) was prepared using the same Fe loading as N@P-Fe2. The co-introduction of Ni significantly enhanced the Fe loading. The surface Fe content from XPS analysis increased from 0.29 at% in N@P-Fe to 0.68 at% in N@P-FeNi, accompanied by a Ni content of 0.20 at% (Table S7). The high-resolution Fe 2p and Ni 2p spectra revealed a pronounced electronic synergy (Figure S9). Compared with their monometallic counterparts, N@P-FeNi exhibited higher fractions of both Fe^{2+} and Ni^{2+} (Table S8). This indicates that the FeNi bimetallic environment promotes the stabilization of metal ions in their active M–N_x coordination states. Among the varied Fe:Ni loading ratios (1:1, 1:2, and 2:1), the 1:1 ratio delivered the highest fractions of pyridinic nitrogen and M–N_x species (Figure S10, Table S9), identifying it as the optimal composition for maximizing the density of active sites.

To probe the electronic interaction between the two metals, the binding energies of the Fe 2p and Ni 2p peaks were compared with those of the monometallic counterparts. N@P-FeNi showed positive shifts of ~0.58 eV for Fe 2p and ~0.70 eV for Ni 2p. Both shifts being in the same positive direction suggests a complex electronic reorganization at the bimetallic interface; analogous co-directional binding energy shifts have

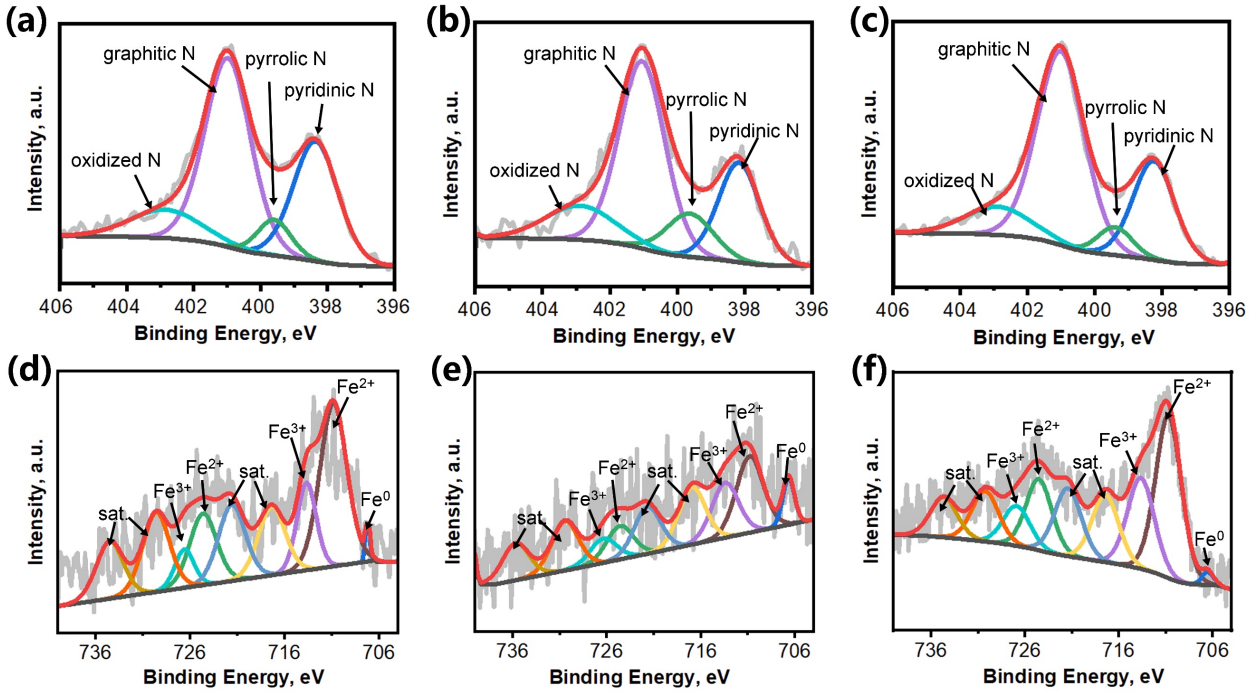

Figure 8. The high-resolution N 1s spectra of (a) N@P, (b) G@P, (c) P@P). The high-resolution Fe 2p spectrum of (d) N@P-Fe, (e) G@P-Fe, (f) P@P-Fe.

been documented in multi-element alloy systems and attributed to multi-body electronic interactions rather than simple pairwise charge transfer [26, 27]. Furthermore, a notable increase in the Ni^{3+} fraction was observed in the bimetallic system. This observation, together with the positive binding energy shift of Ni 2p, indicates a higher oxidation state of Ni in the bimetallic environment. These altered electronic structures may contribute to modulating the d-band center and optimizing the adsorption/desorption behavior of reaction intermediates in ORR and HER [28, 29].

3.3 Electrocatalytic performance

The ORR performance of the metal-loaded core-shell-derived carbons was first evaluated in O_2-saturated 0.1 M KOH electrolyte. All samples displayed featureless voltammetric profiles in N_2-saturated solution. Upon O_2 introduction, well-defined cathodic oxygen reduction peaks emerged, confirming the ORR activity of each catalyst (Figure S11).

The ORR performance of non-core-shell counterparts (N-Fe, G-Fe, and PANI-Fe) was first examined. Their linear sweep voltammetry (LSV) curves revealed that PANI-Fe delivered the best activity among the three non-core-shell catalysts (Figure 9(a)), with an onset potential (E_0) of 1.01 V and a half-wave potential ($E_{1/2}$) of 0.84 V. In comparison, G-Fe exhibited an E_0 of 0.86 V and an $E_{1/2}$ of 0.73 V, while N-Fe showed significantly poorer activity (E_0 = 0.79 V, $E_{1/2}$ = 0.46 V) (Table S10). The Tafel slope increased in the order PANI-Fe (87.25 mV·dec^{-1}) < G-Fe (103.86 mV·dec^{-1}) < N-Fe (116.36 mV·dec^{-1}) (Figure S12), confirming that PANI-Fe possessed the most favorable ORR kinetics among the three samples.

The superior performance of PANI-Fe among the non-core-shell systems can be understood from the intrinsic characteristics of the carbon precursors. PANI, as a nitrogen-rich conjugated polymer, may yield a continuous C–N network upon pyrolysis [30], offering both efficient electron transport pathways and abundant coordination sites for Fe. The NPS-derived carbon (N-Fe), on the other hand, undergoes near-complete decomposition during carbonization. As evidenced by its negligible char yield in TGA, this leaves behind an insufficient carbon scaffold to support active sites. The Glus-derived carbon (G-Fe) retains a carbonaceous framework but is limited by its high oxygen content, low electronic conductivity, and low pyridinic nitrogen fraction, which collectively disfavor the formation of efficient Fe–N_x sites. These results highlight the necessity of a robust, nitrogen-rich carbon matrix for effective Fe-based ORR catalysis. However, none of the individual polymers alone can simultaneously provide a conductive carbon

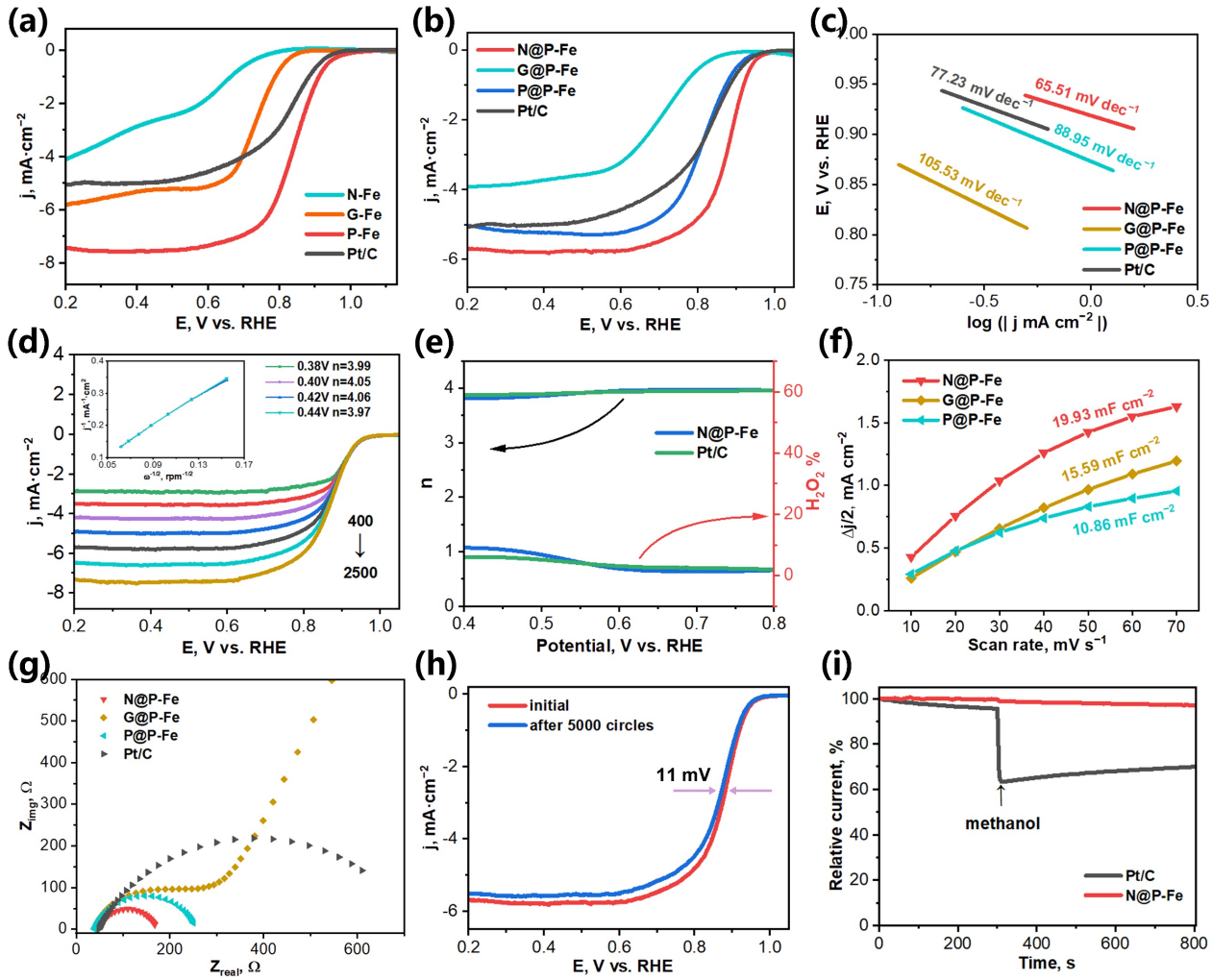

Figure 9. (a) LSV curves of N@P-Fe, G-Fe, P-Fe and Pt/C at a rate of 10 mV·s^{-1} at 1600 rpm. (b) LSV curves of N@P-Fe, G@P-Fe, P@P-Fe and Pt/C at a rate of 10 mV·s^{-1} at 1600 rpm. (c) Tafel plots of N@P-Fe, G@P-Fe, P@P-Fe and Pt/C. (d) LSV curves of N@P-Fe at a series of rotation speeds from 400 to 2500 rpm and the fitted K-L plots at different potentials. (e) H_2O_2 yield and electron transfer number n from the RRDE test of N@P-Fe and Pt/C. (f) Double-layer capacitance (C_{dl}) of N@P-Fe, G@P-Fe, P@P-Fe. (g) Nyquist plots of N@P-Fe, G@P-Fe, P@P-Fe and Pt/C. (h) LSV curves of N@P-Fe before and after 5000 CV cycles. (i) The i-t response curves for the methanol immunity experiments of N@P-Fe and Pt/C.

framework with high pyridinic nitrogen density and sufficient porosity. This limitation motivates the construction of core-shell architectures, where the complementary strengths of different polymers can be synergistically combined.

The construction of core-shell structures markedly enhanced the ORR performance in a core-dependent manner (Figure 9(b)). N@P-Fe exhibited an $E_{1/2}$ of 0.88 V (achieved at the optimal Fe loading of N@P-Fe2), outperforming P@P-Fe ($E_{1/2}$ = 0.82 V), G@P-Fe ($E_{1/2}$ = 0.70 V) and commercial Pt/C. The Tafel slope of N@P-Fe (65.51 mV·dec^{-1}) was the lowest among the three core-shell systems (Figure 9(c)), suggesting more favorable reaction kinetics. As a control, the sequentially synthesized catalysts with distinct core-shell interfaces (NPS-Fe@P and Glus-Fe@P) were also evaluated and both exhibited significantly lower activity than their interpenetrated counterparts (Figure S13). This confirms that intimate interfacial contact is essential for realizing the dynamic core modulation effect.

To gain insight into the ORR kinetics, LSV curves were recorded at various rotation speeds. The electron transfer number (n) was calculated using the Koutecký–Levich (K–L) equation. Both N@P-Fe and P@P-Fe exhibited n values close to 4.0 over the investigated potential range (Figure 9(d) and Figure S14), indicating a dominant four-electron (4e$^-$) ORR pathway. In contrast, G@P-Fe displayed a lower n value of approximately 3.6, suggesting a mixed 2e$^-$/4e$^-$ pathway. Rotating ring-disk electrode (RRDE) measurements yielded results consistent with

the K–L analysis. N@P-Fe maintained an n value near 4.0 across the potential range of 0.4–0.8 V (vs. RHE), accompanied by a H_2O_2 yield below 10% (Figure 9(e)). These results confirmed the high selectivity toward the $4e^-$ pathway.

The electrochemically active surface area (ECSA) was evaluated by measuring the double-layer capacitance (C_{dl}) from CV curves recorded at different scan rates (Figure S15). N@P-Fe exhibited the largest C_{dl} among the three core-shell systems, indicating the highest density of accessible active sites (Figure 9(f)). N@P-Fe2 achieved the maximum C_{dl} of 19.93 $mF{\cdot}cm^{-2}$ (Figure S16), consistent with its optimal Fe–N_x site configuration. Electrochemical impedance spectroscopy (EIS) measurements also showed that N@P-Fe possessed the smallest charge transfer resistance (R_{ct}) among the three systems (Figure 9(g)), reflecting the most efficient electron transport.

The durability and methanol tolerance of N@P-Fe were evaluated using accelerated degradation and chronoamperometric tests. After 5000 CV cycles at a scan rate of 100 $mV{\cdot}s^{-1}$, the $E_{1/2}$ of N@P-Fe decayed by only 11 mV (Figure 9(h)). Upon the addition of methanol (3 M) at 300 s during chronoamperometry, N@P-Fe showed a current attenuation of less than 3%, whereas Pt/C suffered an approximately 40% loss (Figure 9(i)). TEM images of N@P-Fe after the 5000-cycle stability test revealed no discernible morphological change. The elemental mapping confirmed that Fe remained uniformly distributed (Figure S17).

Encouraged by the excellent ORR performance of the N@P-Fe system, we extended the core-to-shell modulation strategy to a bimetallic FeNi configuration. The optimized N@P-FeNi catalyst (Fe:Ni = 1:1) exhibited further improved ORR activity (Figure 10(a, b) and Figure S18), with an E_0 of 1.00 V, an $E_{1/2}$ of 0.89 V, and a limiting current density (j_L) of 6.46 $mA{\cdot}cm^{-2}$. All these metrics surpassed those of its monometallic counterpart N@P-Fe2. The performance of N@P-FeNi is also competitive with and even surpasses many recently reported core-shell or N-doped carbon encapsulated Fe-based catalysts (Table S11) [31–42], such as F127-mediated Fe/N-doped core-shell carbons ($E_{1/2}$ = 0.87 V) [32], N, S co-doped carbon shell encapsulating Fe_5C_2 nanoparticles ($E_{1/2}$ = 0.86 V) [33], hierarchically porous FeNi-NPC-1000 ($E_{1/2}$ = 0.877 V) [34].

The Tafel slope of N@P-FeNi decreased to 62.6 $mV{\cdot}dec^{-1}$, consistent with its enhanced ORR activity (Figure 10(c)). K–L analysis yielded an n value of 3.83, and RRDE measurements confirmed an n value of 3.95–4.00 across 0.4–0.8 V (vs. RHE), with a H_2O_2 yield consistently below 9% (Figure S19). The C_{dl} of N@P-FeNi reached 20.45 $mF{\cdot}cm^{-2}$ (Figure 10(d)), exceeding that of N@P-Fe. EIS measurements revealed that N@P-FeNi exhibited the smallest semicircle diameter at the same potential, significantly lower than that of N@P-Fe (Figure S20(a)). These results indicate an increased density of active sites and substantially enhanced charge transfer efficiency in the bimetallic system. Durability tests further demonstrated the robustness of the bimetallic system. After 5000 CV cycles, the $E_{1/2}$ of N@P-FeNi decayed by only 7 mV, outperforming N@P-Fe (11 mV) (Figure S20(b)). Methanol tolerance tests showed similarly negligible current attenuation (Figure S20(c)).

The HER performance of N@P-FeNi was evaluated in 1 M KOH (Figure 10). At a current density of 10 $mA{\cdot}cm^{-2}$, N@P-FeNi delivered an overpotential of 298 mV, markedly lower than that of N@P-Fe (362 mV). This significant improvement in HER activity can be attributed to the electronic synergy between Fe and Ni. The altered electronic structure likely optimizes the hydrogen adsorption free energy, facilitating the HER process.

The superior ORR activity of N@P-Fe can be traced to the synergistic interplay in the unique core-shell design. The highly ordered carbon network provides efficient pathways for electron transport to the active sites. This conductive framework is populated by a high density of atomically dispersed Fe–N_x sites anchored at pyridinic nitrogen. Complementing these electronic and structural attributes, the well-developed hierarchical pore structure ensures that these active sites are readily accessible to reactants through efficient mass transport. The dynamic pyrolysis behavior of the NPS core, through its early decomposition and interfacial restructuring, creates the essential structural and chemical environment that enables the optimization for enhanced activity. The dependence of ORR activity on Fe loading further reinforces the existence of an optimal balance between active site density and metal dispersion, an insight made possible by the systematic tunability of the core-shell platform. The electronic synergy between Fe and Ni in the bimetallic N@P-FeNi system not only improves the intrinsic activity of the active sites but also enhances catalyst stability and bifunctional ORR/HER performance.

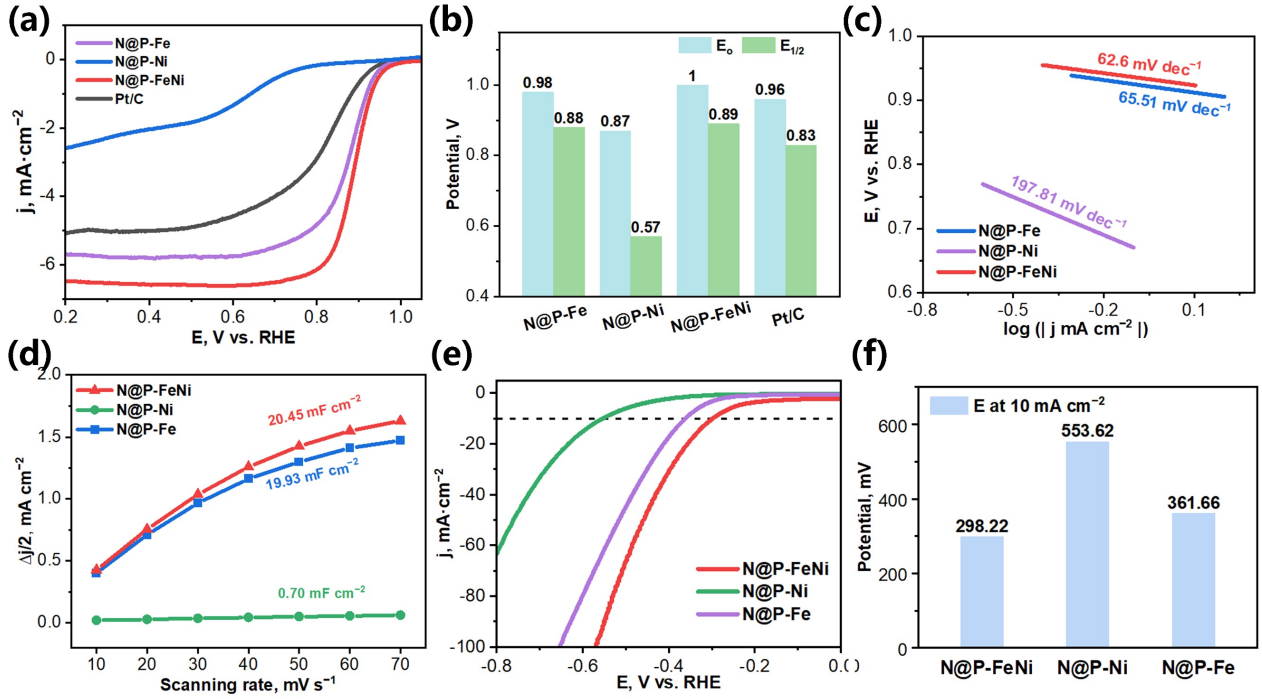

Figure 10. (a) LSV curves of N@P-Fe, N@P-Ni, N@P-FeNi and Pt/C at a rate of 10 mV·s^{-1} at 1600 rpm. (b) The comparison of E_o and $E_{1/2}$ of N@P-Fe, N@P-Ni, N@P-FeNi and Pt/C. (c) Tafel plots, (d) double-layer capacitance (C_{dl}) of N@P-Fe, N@P-Ni, and N@P-FeNi. (e) HER polarization curves of N@P-Fe, N@P-Ni, and N@P-FeNi in 1 M KOH. (f) The corresponding overpotentials at 10 mA·cm^{-2} for the three catalysts.

These demonstrations underscore the versatility of the core-to-shell modulation approach for developing multi-functional carbon-based electrocatalysts. It is important to note that our catalyst is prepared via a straightforward, polymer-based approach without complex templates or HF etching, which offers a compelling balance between exceptional catalytic performance and synthetic practicality.

4 Conclusion

In summary, we have demonstrated that the core polymer in core-shell structured systems plays a dynamic regulatory role during pyrolysis. By systematically comparing three core polymers coated with an identical PANI shell, we showed that the nitrogen-rich NPS core, undergoing pronounced volume change, remotely modulates the carbonization pathway of the shell. This effect promotes the formation of a more ordered carbon framework with a higher density of pyridinic nitrogen, which in turn facilitates the stabilization of Fe as atomically dispersed Fe–N_x active sites. The resultant N@P-Fe catalyst exhibits superior ORR performance, outperforming both Fe-loaded single-polymer-derived carbons and commercial Pt/C. The generality of this core-to-shell modulation strategy was further validated by extending it to a bimetallic FeNi system, which delivered enhanced bifunctional ORR/HER performance with an ORR $E_{1/2}$ of 0.89 V and an HER overpotential of 298 mV at 10 mA·cm^{-2}. This work demonstrates that engineering the dynamic pyrolysis behavior of the core can effectively combine synthetic simplicity with competitive catalytic performance, offering a new dimension for the rational design of polymer-derived carbon electrocatalysts.

Data Availability Statement

Data will be made available on request.

Funding

This work was supported by the Instrument & Equipment Open Funding of Nanjing University of Science and Technology, China, and the National Natural Science Foundation of China under Grant 22338003.

Conflicts of Interest

The authors declare no conflicts of interest.

AI Use Statement

The authors declare that Deepseek-V3 was used for

proofreading of the entire manuscript. The authors have carefully reviewed, revised, and verified the AI-assisted output and take full responsibility for the content of the manuscript.

Ethical Approval and Consent to Participate

Not applicable.

References

[1] Zhao, Z., Sun, L., Li, Y., & Feng, W. (2023). Polymer-derived carbon materials for energy storage devices: A mini review. *Carbon, 210*, 118066. [CrossRef]

[2] Li, W., Wang, C., & Lu, X. (2022). Conducting polymers-derived fascinating electrocatalysts for advanced hydrogen and oxygen electrocatalysis. *Coordination Chemistry Reviews, 464*, 214555. [CrossRef]

[3] Li, K., Meng, F., Li, J., Wu, H., Jia, H., & Ji, Q. (2026). Engineering accessible Fe-N sites in polypyrrole-derived-catalysts via a dynamic coordination strategy. *Sustainable Energy Fuels, 10*, 587-595. [CrossRef]

[4] Wu, H., Li, J., Ji, Q., & Ariga, K. (2024). Nanoarchitectonics for structural tailoring of yolk-shell architectures for electrochemical applications. *Science and Technology of Advanced Materials, 25*, 2420664. [CrossRef]

[5] Jones, C. F., Resina, L., Ferreira, F. C., Sanjuan-Alberte, P., & Esteves, T. (2024). Conductive core–shell nanoparticles: Synthesis and applications. *Journal of Physical Chemistry C, 128*(27), 11083-11100. [CrossRef]

[6] Das, S., Pérez-Ramírez, J., Gong, J., Dewangan, N., Hidajat, K., Gates, B. C., & Kawi, S. (2020). Core-shell structured catalysts for thermocatalytic, photocatalytic, and electrocatalytic conversion of CO2. *Chemical Society Reviews, 49*, 2937-3004. [CrossRef]

[7] Nguyen, Q. H., Im, K., & Kim, J. (2022). Synthesis of hollow Fe, Co, and N-doped carbon catalysts from conducting polymer-metal-organic-frameworks core-shell particles for their application in an oxygen reduction reaction. *International Journal of Hydrogen Energy, 47*, 24169-24178. [CrossRef]

[8] Jiao, S., Li, C., Zhang, Y., Li, Z., Liu, K., & Wang, L. (2023). ZIF-8-templated synthesis of core-shell structured IPOP@MOF hybrid-derived nitrogen-doped porous carbon for efficient oxygen reduction electrocatalysis and supercapacitor. *Electrochimica Acta, 441*, 141817. [CrossRef]

[9] Campos-Roldan, C. A., Gonzalez-Huerta, G., & Alonso-Vante, N. (2018). Experimental protocol for HOR and ORR in alkaline electrochemical measurements. *Journal of The Electrochemical Society, 165*, J3001. [CrossRef]

[10] Márquez, R. A., Kawashima, K., Son, Y. J., Castelino, G., Miller, N., Smith, L. A., Chukwuneke, C. E., & Mullins, C. B. (2023). Getting the basics right: Preparing alkaline electrolytes for electrochemical applications. *ACS Energy Letters, 8*(2), 1141-1146. [CrossRef]

[11] Ding, D., Gao, F., Wu, Y., Li, Y., Li, T., & Ren, B. (2023). Preparation and electrochemical application of melamine resin-based carbon materials. *Journal of Porous Materials, 30*, 1319-1335. [CrossRef]

[12] Rao, L., Ma, R., Liu, S., Wang, L., Wu, Z., Yang, J., & Hu, X. (2019). Nitrogen enriched porous carbons from d-glucose with excellent CO2 capture performance. *Chemical Engineering Journal, 362*, 794-801. [CrossRef]

[13] Xie, N.-H., Yan, X.-H., & Xu, B.-Q. (2016). Is ammonium peroxydisulfate indispensable for preparation of aniline-derived iron–nitrogen–carbon electrocatalysts. *ChemSusChem, 9*, 2301-2306. [CrossRef]

[14] Ullah, S., Bustam, M. A., Nadeem, M., Naz, M. Y., Tan, W. L., & Shariff, A. M. (2014). Synthesis and thermal degradation studies of melamine formaldehyde resins. *Scientific World Journal, 2014*, 940502. [CrossRef]

[15] Akula, S., & Sahu, A. K. (2020). Structurally modulated graphitic carbon nanofiber and heteroatom (N,F) engineering toward metal-free ORR electrocatalysts for polymer electrolyte membrane fuel cells. *ACS Applied Materials & Interfaces, 12*, 11438-11449. [CrossRef]

[16] Bora, N., Joshi, D. P., & Aulakh, J. S. (2024). Influence of polyaniline conducting polymer on thermal properties of phase change material for thermal energy storage. *Polymer Bulletin, 81*, 1597–1621. [CrossRef]

[17] Nobrega, M. M., Silva, H. B., Constantino, V. R. L., & Temperini, M. L. A. (2012). Spectroscopic study on the structural differences of thermally induced cross-linking segments in emeraldine salt and base forms of polyaniline. *Journal of Physical Chemistry B, 116*(48), 14191-14200. [CrossRef]

[18] Song, W., Xiao, C., Ding, J., Huang, Z., Yang, X., Zhang, T., Mitlin, D., & Hu, W. (2024). Review of carbon support coordination environments for single metal atom electrocatalysts (SACS). *Advanced Materials, 36*, 2301477. [CrossRef]

[19] Wang, J., Bai, J., Cang, Y., Li, Q., Fan, X., & Lin, H. (2023). Noble metal single-atom coordinated to nitrogen, oxygen, and carbon as electrocatalysts for oxygen evolution. *Catalysts, 13*(10), 1378. [CrossRef]

[20] Wang, W., Zuo, X., Yang, Q., Tang, H., Zhang, H., & Li, G. (2022). Constructing Fe/Fe3C nanocrystals with Fe-Nx sites in Fe–N–C electrocatalyst to achieve high performance for solar cells. *Applied Catalysis B: Environmental, 300*, 120726. [CrossRef]

[21] Tian, Y., Xu, L., Qian, J., Bao, J., Yan, C., Li, H., Li, H., & Zhang, S. (2019). Fe3C/Fe2O3 heterostructure

embedded in N-doped graphene as a bifunctional catalyst for quasi-solid-state zinc–air batteries. *Carbon, 146*, 763-771. [CrossRef]

[22] Wei, J., Xia, D., Wei, Y., Zhu, X., Li, J., & Gan, L. (2022). Probing the oxygen reduction reaction intermediates and dynamic active site structures of molecular and pyrolyzed Fe–N–C electrocatalysts by in situ Raman spectroscopy. *ACS Catalysis, 12*, 7811–7820. [CrossRef]

[23] Zhou, Y., Yu, Y., Ma, D., Foucher, A. C., Xiong, L., Zhang, J., Stach, E. A., Yue, Q., & Kang, Y. (2021). Atomic Fe dispersed hierarchical mesoporous Fe–N–C nanostructures for an efficient oxygen reduction reaction. *ACS Catalysis, 11*, 74–81. [CrossRef]

[24] Xu, H., Li, R., Li, Y., Lu, X., Liu, H., Yang, P., & Bai, J. (2025). Research progress of atomically dispersed iron, nitrogen co-coordinated carbon catalysts for oxygen reduction: a mini-review. *Journal of Materials Chemistry A, 13*, 13675-13692. [CrossRef]

[25] Zhou, Y., Mao, Y., Chang, M., Wang, Z., Xie, W., Ye, C., Wei, S., Thomsen, L., & Waterhouse, G. I. N. (2026). Tuning the electronic structure and spin state of Fe-N-C catalysts using an axial oxygen ligand and Fe clusters for high-efficiency rechargeable zinc–air batteries. *Advanced Functional Materials, 36*, e19133. [CrossRef]

[26] Xu, X., Guo, Y., Bloom, B. P., Wei, J., Li, H., Li, H., Du, Y., Zeng, Z., Li, L., & Waldeck, D. H. (2020). Elemental core level shift in high entropy alloy nanoparticles via X-ray photoelectron spectroscopy analysis and first-principles calculation. *ACS Nano, 14*, 17704–17712. [CrossRef]

[27] Wu, J., Ma, Z., Yu, L., Wang, S., Yang, F., & Feng, L. (2024). Phase and chemical state tuning of FeNi oxides for oxygen evolution reaction. *Science China Chemistry, 67*, 2755–2766. [CrossRef]

[28] Zhang, W., Yi, S., Yu, Y., Liu, H., Kucernak, A., Wu, J., & Li, S. (2024). Fe-based dual-atom catalysts for the oxygen reduction reaction. *Journal of Materials Chemistry A, 12*, 87-112. [CrossRef]

[29] Zhang, L., Li, B., Xu, H.-Y., Shan, L.-W., & Dong, L.-M. (2026). Modulation strategies of d-band center for HER and AOPs applications: a comprehensive review. *Inorganic Chemistry Frontiers, 13*, 1739-1765. [CrossRef]

[30] Kuroki, S., Hosaka, Y., & Yamauchi, C. (2013). A solid-state NMR study of the carbonization of polyaniline. *Carbon, 55*, 160-167. [CrossRef]

[31] Yu, H., Liu, D., Srinivas, K., Ma, F., Zhang, Z., Wang, M., Wu, Y., Wang, Y., Li, X., & Chen, Y. (2023). Core-shell Fe/Fe3C heterostructure@carbon layers anchored on N-doped porous carbon for boosting oxygen reduction reaction. *Journal of Alloys and Compounds, 949*, 169863. [CrossRef]

[32] Zhou, J., Tang, Y., Zhang, L., Yang, H., He, X., Wu, H., Zhang, Y., & Zhou, A. (2025). F127-mediated synthesis of hierarchical core–shell Fe/N-Doped carbon catalyst for enhanced oxygen reduction reaction. *Ionics, 31*, 13175-13186. [CrossRef]

[33] Xiao, L., Yu, W., Liu, J., Luan, S., Li, S., Cui, X., & Jiang, L. (2024). Boosting Oxygen Reduction Reaction via N, S-Doped Carbon Shell Encapsulated Fe5C2: Leveraging Lateral and Axial Synergy. *ACS Sustainable Chemistry & Engineering, 12*, 4709-4717. [CrossRef]

[34] He, Y., Yang, J., Wang, Y., Jia, Y., Li, H., Liu, Y., Liu, L., & Tan, Q. (2024). Atomically dispersed dual-metal ORR catalyst with hierarchical porous structure for Zn–air batteries. *ACS Applied Materials & Interfaces, 16*, 12398-12406. [CrossRef]

[35] Song, J., Ren, Y., Li, J., Huang, X., Cheng, F., Tang, Y., & Wang, H. (2018). Core-shell Co/CoNx@C nanoparticles enfolded by Co-N doped carbon nanosheets as a highly efficient electrocatalyst for oxygen reduction reaction. *Carbon, 138*, 300-308. [CrossRef]

[36] Li, S., Miao, W., Lv, E., Cao, X., Li, X., Zhang, X., Yu, H., & Dong, X. (2022). High-performance ORR Catalyst of N-doping Carbon-coated Cobalt Nanoparticles Synthesized by DC Arc Plasma. *ChemistrySelect, 7*, e202201823. [CrossRef]

[37] Wang, D., Wang, Q., Jiang, S., Dong, K., Wang, Z., Luo, S., Liu, Y., Zhang, Y., Wang, Q., & Yi, T. (2020). NiCo alloy nanoparticles encapsulated in N-doped 3D porous carbon as efficient electrocatalysts for oxygen reduction reaction. *International Journal of Hydrogen Energy, 45*, 22797-22807. [CrossRef]

[38] Cao, X., Miao, W., Qin, M., Lv, E., Yu, H., Zhang, X., & Dong, X. (2023). N-doping carbon-coated Cu@C(N) nanocapsules synthesized by arc plasma toward high-performance ORR electrocatalyst. *Journal of Alloys and Compounds, 948*, 169739. [CrossRef]

[39] Quan, L., Yu, X., Wang, T., Yin, W., Liu, J., Wang, L., & Zhang, Y. (2019). Ultrafine Co@nitrogen-doped carbon core-shell nanostructures anchored on carbon nanotubes for highly efficient oxygen reduction. *Applied Surface Science, 494*, 691-699. [CrossRef]

[40] Wang, H., Wang, W., Xu, Y. Y., Dong, S., Xiao, J., Wang, F., Liu, H., & Xia, B. Y. (2017). Hollow nitrogen-Doped carbon spheres with Fe3O4 nanoparticles encapsulated as a highly active oxygen-reduction catalyst. *ACS Applied Materials & Interfaces, 9*, 10610-10617. [CrossRef]

[41] Wu, M., Xie, J., Liu, A., Jia, W., & Cao, Y. (2020). Iron carbide/nitrogen-doped carbon core-shell nanostructures: Solution-free synthesis and superior oxygen reduction performance. *Journal of Colloid and Interface Science, 566*, 194-201. [CrossRef]

[42] Liu, S., Wang, Z., Zhou, S., Yu, F., Yu, M., Chiang, C.-Y., Zhou, W., Zhao, J., & Qiu, J. (2017). Metal–organic-framework-derived hybrid carbon nanocages as a bifunctional electrocatalyst for oxygen reduction and evolution. *Advanced Materials, 29*, 1700874. [CrossRef]

Additional Data

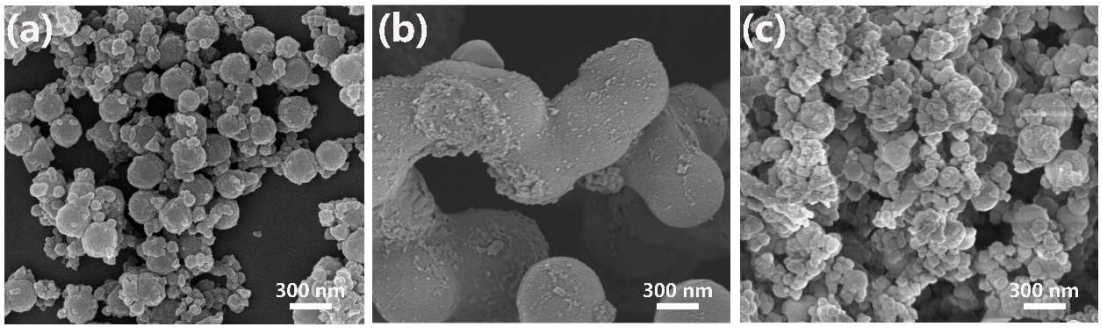

Figure S1. SEM images of the core-shell precursors with Fe^{3+} before pyrolysis, (a) NPS@PANI-Fe, (b) GluS@PANI-Fe and (c) PANI@PANI-Fe.

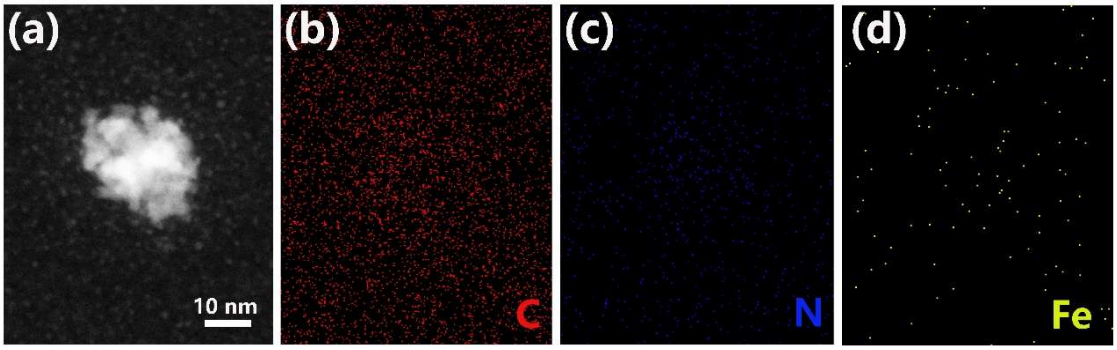

Figure S2. (a) HAADF-STEM and (b-d) corresponded EDS-mapping images of N@P-Fe.

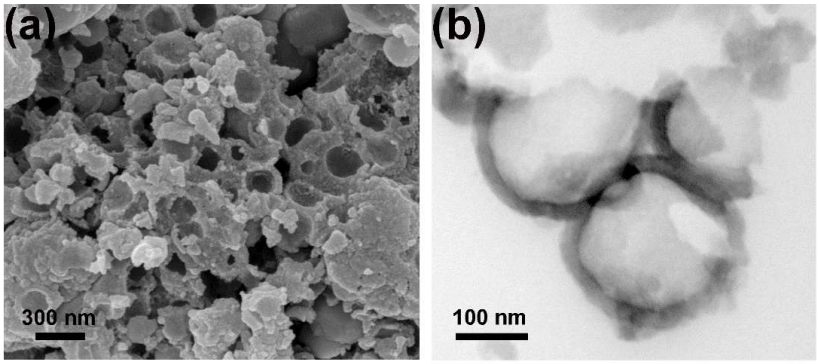

Figure S3. (a) SEM and (b) TEM images of NPS-Fe@P. The samples were prepared by first loading Fe within NPS core, followed by PANI shell polymerization and subsequent pyrolysis.

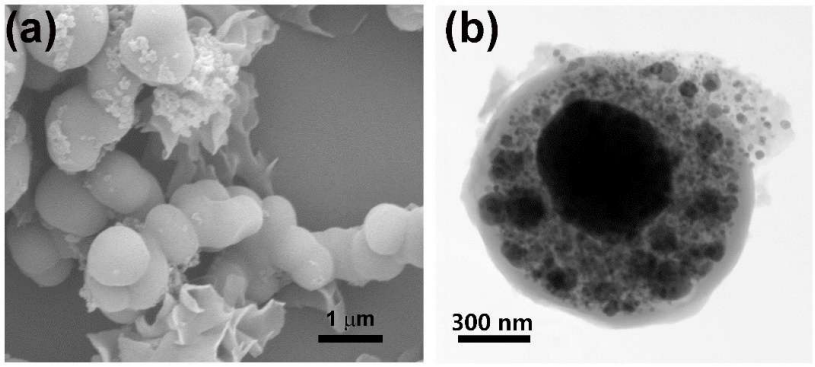

Figure S4. (a) SEM and (b) TEM images of GluS-Fe@P. The samples were prepared by first loading Fe within GluS core, followed by PANI shell polymerization and subsequent pyrolysis.

Table S1. The porous features of the prepared carbons from N_2 sorption measurement.

Sample	Specific surface area ($m^2\ g^{-1}$)	Pore volume ($cm^3\ g^{-1}$)	Average pore diameter (nm)
N@P	963.4	0.35	12.6
G@P	463.4	0.18	8.9
P@P	255.5	0.11	10.2

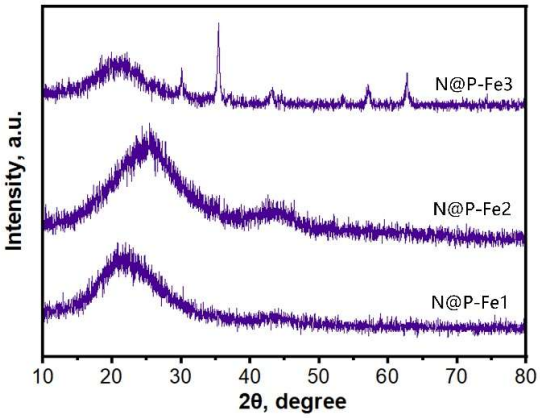

Figure S5. XRD patterns of N@P-Fe with different Fe loading amounts, N@P-Fe1 (Fe:aniline =1:16), N@P-Fe2, (Fe:aniline =1:6), and N@P-Fe3, (Fe:aniline =1:4).

Table S2. The fitted Raman D and G band intensity ratios of the derived carbons from core-shell precursors with and without Fe doping.

Samples	D^1 (%)	D^4 (%)	D^3 (%)	G (%)	D^3/G
N@P	56.07	4.07	14.15	25.71	0.589
G@P	56.10	5.87	15.85	22.18	0.714
P@P	57.39	5.12	14.01	23.48	0.597
N@P-Fe	55.93	6.60	12.48	24.99	0.499
G@P-Fe	54.12	8.35	15.59	21.94	0.711
P@P-Fe	57.63	5.69	13.01	23.67	0.550

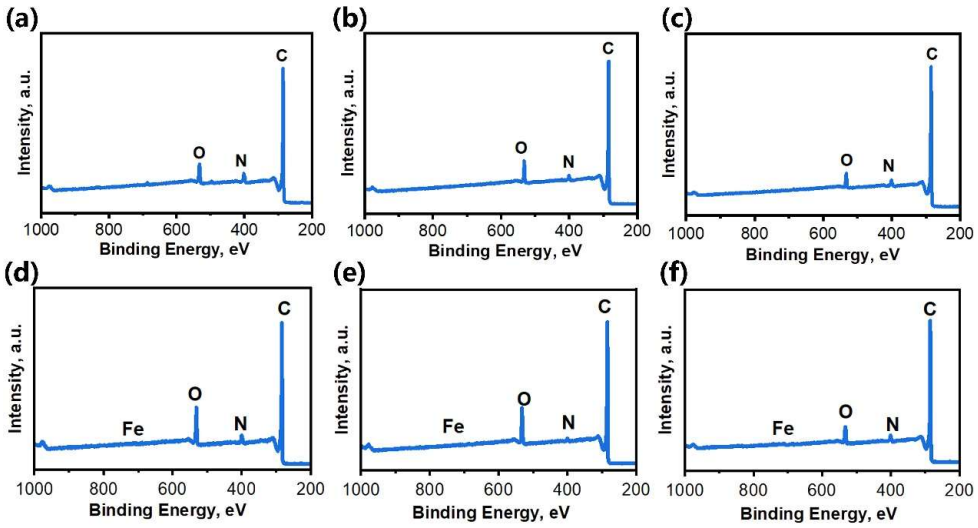

Figure S6. XPS survey spectra of (a) N@P, (b) G@P, (c) P@P, (d) N@P-Fe, (e) G@P-Fe, and (f) P@P-Fe.

Table S3. The elemental compositions and contents of the derived carbons from core-shell precursors with and without Fe doping (based on XPS results).

Sample	C (at.%)	O (at.%)	N (at.%)	Fe (at.%)
N@P	87.29	7.14	5.57	–
G@P	90.9	6.42	2.68	–
P@P	90.7	5.36	3.94	–
N@P-Fe	84.57	10.64	4.5	0.29
G@P-Fe	88.11	9.87	1.84	0.18
P@P-Fe	90.27	6.04	3.3	0.39

Table S4. The relative content and type of N in the derived carbons from core-shell precursors with and without Fe doping (calculated based on XPS results).

Sample	pyridinic N (%)	Fe–N (%)	pyrrolic N (%)	graphitic N (%)	oxidized N (%)
N@P	31.04	–	6.84	50.36	11.76
G@P	24.18	–	11.79	50.00	14.03
P@P	25.39	–	5.96	57.09	11.56
N@P-Fe1	21.78	10.44	28.75	30.72	8.31
N@P-Fe (N@P-Fe2)	25.41	16.31	22.76	24.98	10.54
N@P-Fe3	24.77	11.90	22.57	33.15	7.61
G@P-Fe	23.84	10.89	28.14	20.35	16.78
P@P-Fe	23.34	13.48	24.78	30.23	8.17

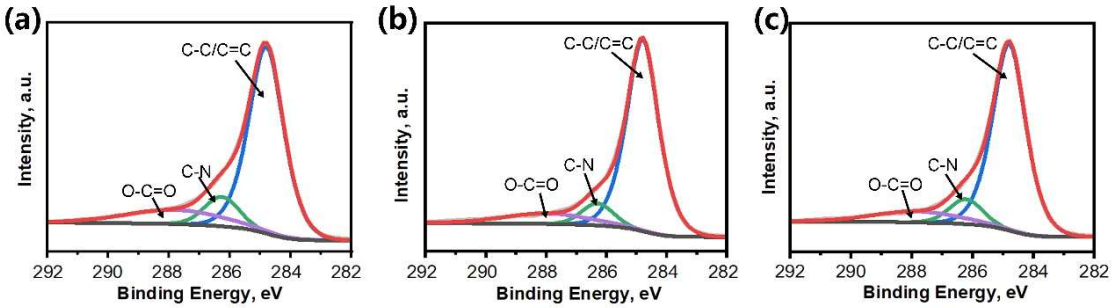

Figure S7. The high-resolution C 1s spectra of (a) N@P, (b) G@P, (c) P@P.

Table S5. The relative content and type of C in the derived carbons from core-shell precursors with and without Fe doping (calculated based on XPS results).

Samples	C–C (%)	C–N (%)	O=C–O (%)
N@P	73.41	11.19	15.40
G@P	79.88	8.72	11.40
P@P	78.52	9.94	11.54

Table S6. The relative contents of Fe species in the derived carbons from core-shell precursors with Fe doping (calculated based on XPS results).

Samples	Fe^{2+} (%)	Fe^{3+} (%)	Fe^{0} (%)
N@P-Fe1	55.94	32.7	11.36
N@P-Fe (N@P-Fe2)	71.27	27.03	1.70
N@P-Fe3	64.88	27.54	7.58
G@P-Fe	52.53	37.76	9.71
P@P-Fe	62.27	36.19	1.54

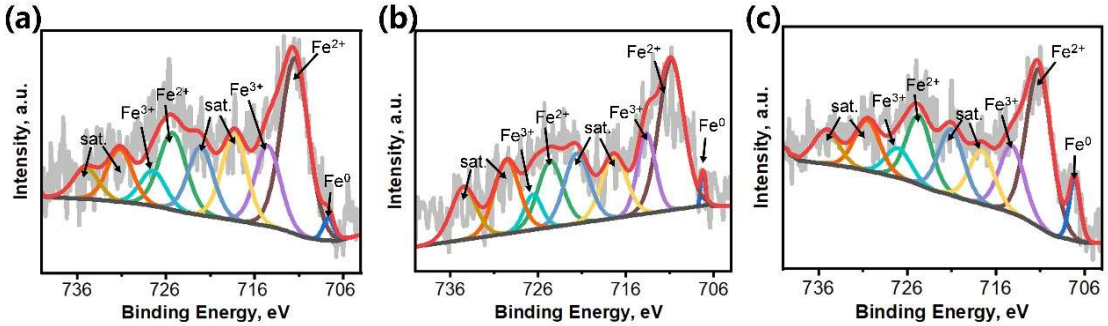

Figure S8. The high-resolution Fe 2p spectra of (a) N@P-Fe1, (b) N@P-Fe2, and (c) N@P-Fe3.

Table S7. The elemental compositions and contents of N@P-FeNi, N@P-Fe, and N@P-Ni (based on XPS results).

Sample	C (at.%)	O (at.%)	N (at.%)	Fe (at.%)	Ni (at.%)
N@P-FeNi	81.36	11.3	6.46	0.68	0.20
N@P-Fe	84.57	10.64	4.50	0.29	–
N@P-Ni	86.11	7.54	6.13	–	0.21

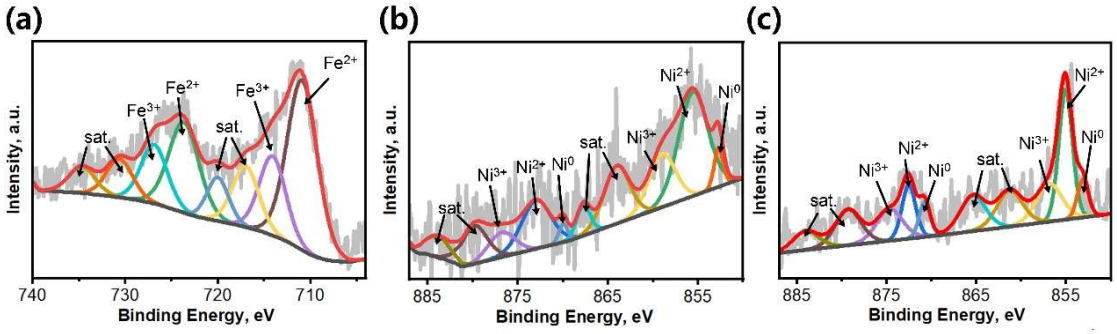

Figure S9. (a) The high-resolution Fe 2p spectra of N@P-FeNi. The high-resolution Ni 2p spectra of (b) N@P-FeNi, and (c) N@P-Ni.

Table S8. The relative contents of Fe and Ni species in N@P-FeNi, N@P-Fe, and N@P-Ni (calculated based on XPS results).

Samples	Fe^{2+} (%)	Fe^{3+} (%)	Fe^{0} (%)	Ni^{2+} (%)	Ni^{3+} (%)	Ni^{0} (%)
N@P-FeNi1:2	68.65	30.57	0.78	54.35	14.71	30.94
N@P-FeNi (N@P-FeNi1:1)	70.91	29.09	0.00	63.64	29.22	7.14
N@P-FeNi2:1	64.74	31.73	3.53	57.20	40.15	2.65
N@P-Fe	71.27	27.03	1.70	–	–	–
N@P-Ni	–	–	–	55.69	31.21	13.1

Table S9. The relative content and type of N in N@P-FeNi, N@P-Fe and N@P-Ni (calculated based on XPS results).

Sample	pyridinic N (%)	M–N_x (%)	pyrrolic N (%)	graphitic N (%)	oxidized N (%)
N@P-FeNi-1:2	22.12	13.68	29.16	23.12	11.92
N@P-FeNi (N@P-FeNi-1:1)	28.99	23.97	27.6	17.1	2.34
N@P-FeNi-2:1	25.66	15.54	32.03	14.83	11.94
N@P-Fe	25.41	16.31	22.76	24.98	10.54
N@P-Ni	27.96	14.61	26.17	27.68	3.58

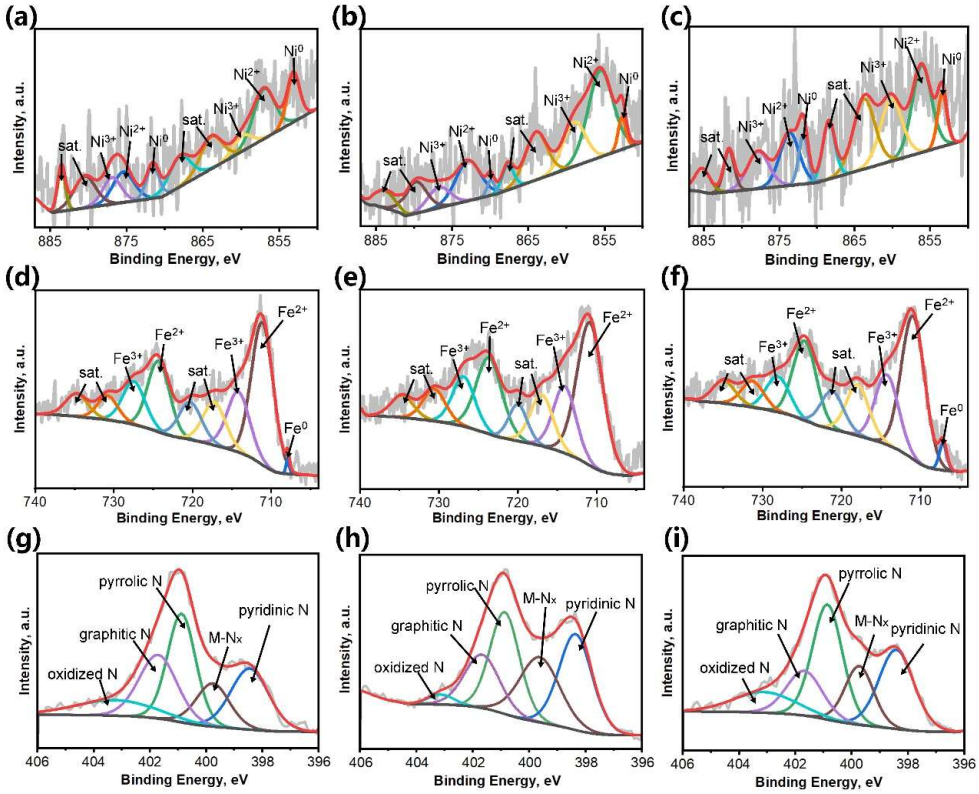

Figure S10. The high-resolution Ni 2p spectra of (a) N@P-FeNi-1:2, (b) N@P-FeNi-1:1, (c) N@P-FeNi-2:1. The high-resolution Fe 2p spectra of (d) N@P-FeNi-1:2, (e) N@P-FeNi-1:1, (f) N@P-FeNi-2:1. The high-resolution N 1s spectra of (g) N@P-FeNi-1:2, (h) N@P-FeNi-1:1, (i) N@P-FeNi-2:1..

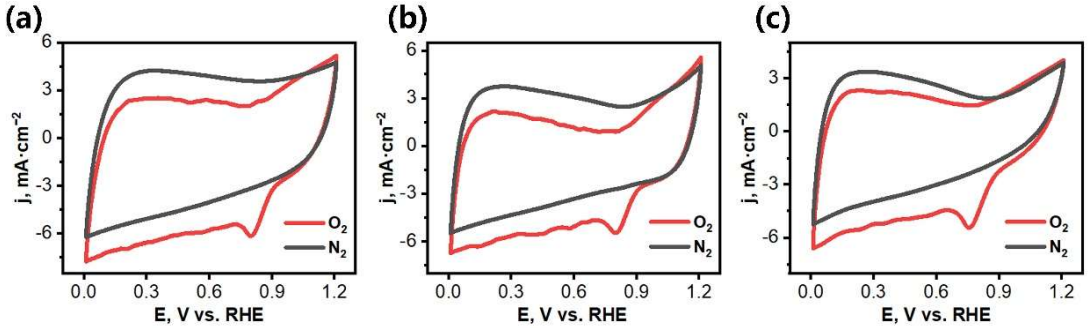

Figure S11. CV curves of (a) N@P-Fe, (b) G@P-Fe and (c) P@P-Fe in N_2 and O_2 saturated 0.1 M KOH solution at a scan rate of 50 mV·s^{-1}.

Table S10. ORR performance comparison of Fe-loaded single-polymer-derived carbons (N-Fe, G-Fe, P-Fe), the corresponding core-shell-derived carbons (N@P-Fe, G@P-Fe, P@P-Fe) and Pt/C.

Sample	E_0 (V)	$E_{1/2}$ (V)	j_L (mA·cm^{-2})
N-Fe	0.79	0.46	4.05
G-Fe	0.86	0.73	5.84
P-Fe	1.01	0.84	7.42
N@P-Fe	0.98	0.88	5.67
G@P-Fe	0.88	0.7	3.91
P@P-Fe	0.96	0.82	5.05
Pt/C	0.96	0.84	5.07

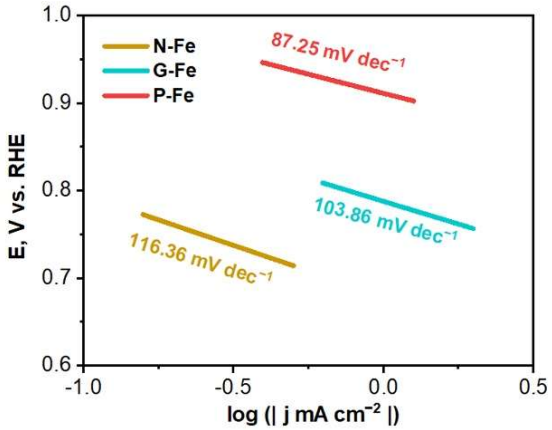

Figure S12. Tafel plots of N-Fe, G-Fe, P-Fe.

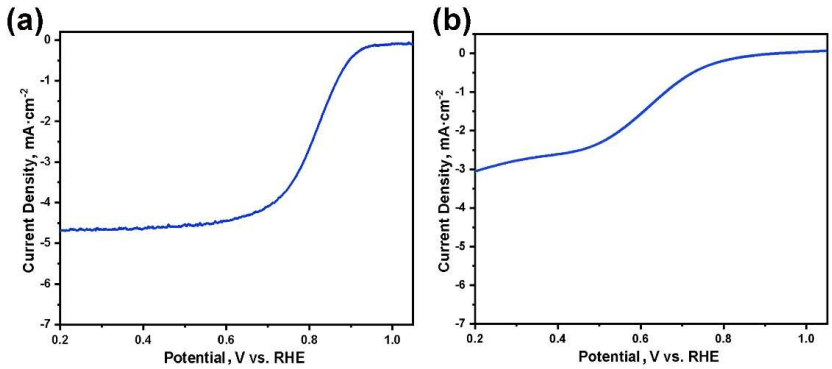

Figure S13. LSV curves of (a) NPS-Fe@P and (b) GluS-Fe@P at a rate of 10mV·s^{-1} at 1600 rpm.

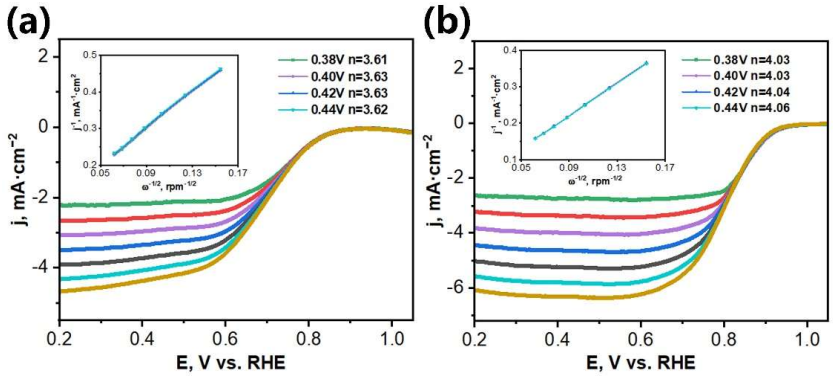

Figure S14. LSV curves of (a) G@P-Fe and (b) P@P-Fe at a series of rotation speeds from 400 to 2500 rpm and the fitted K-L plots at different potentials.

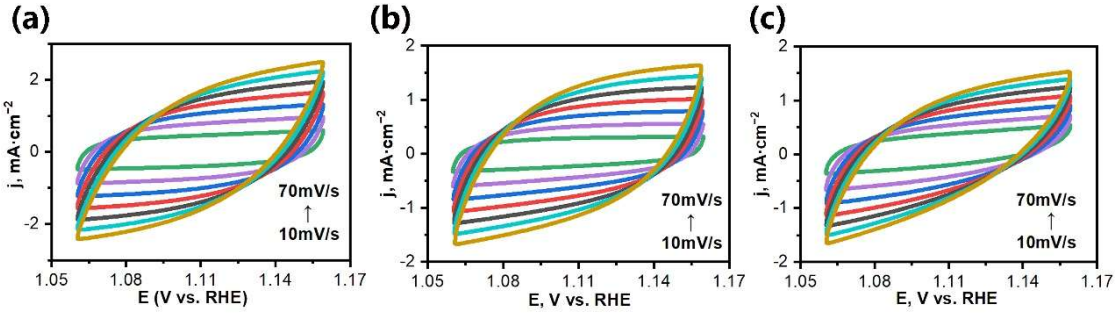

Figure S15. CV curves of (a) N@P-Fe, (b) G@P-Fe, and (c) P@P-Fe in the non-Faradaic potential range of 1.05-1.15 V at scan rates of 10–70 mV·s^{-1}.

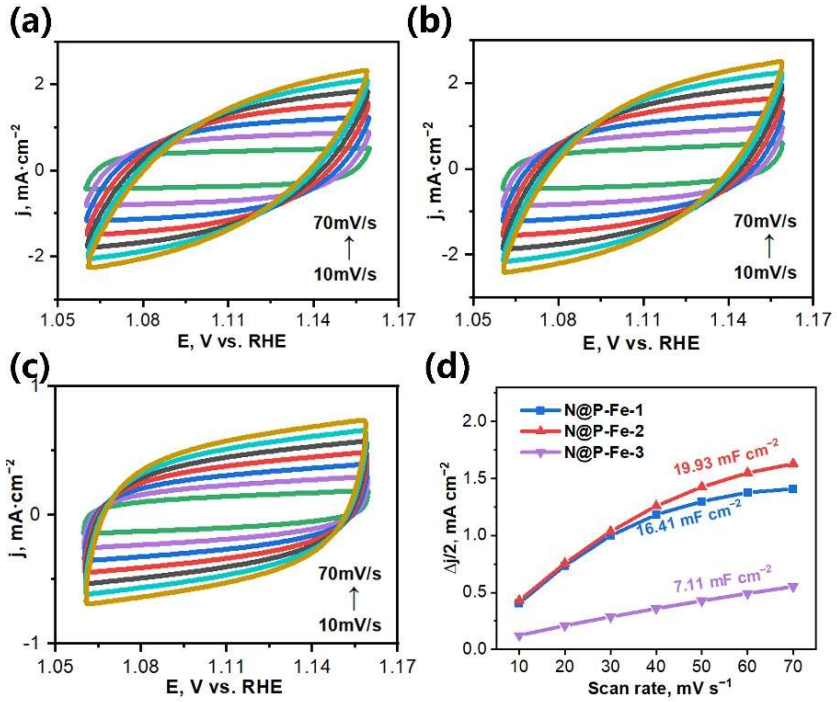

Figure S16. CV curves of (a) N@P-Fe1, (b) N@P-Fe2, and (c) N@P-Fe3 in the non-Faradaic potential range of 1.05-1.15 V at scan rates of 10–70 mV·s^{-1}. (d) Double-layer capacitance (Cdl) of N@P-Fe1, N@P-Fe2, and N@P-Fe3.

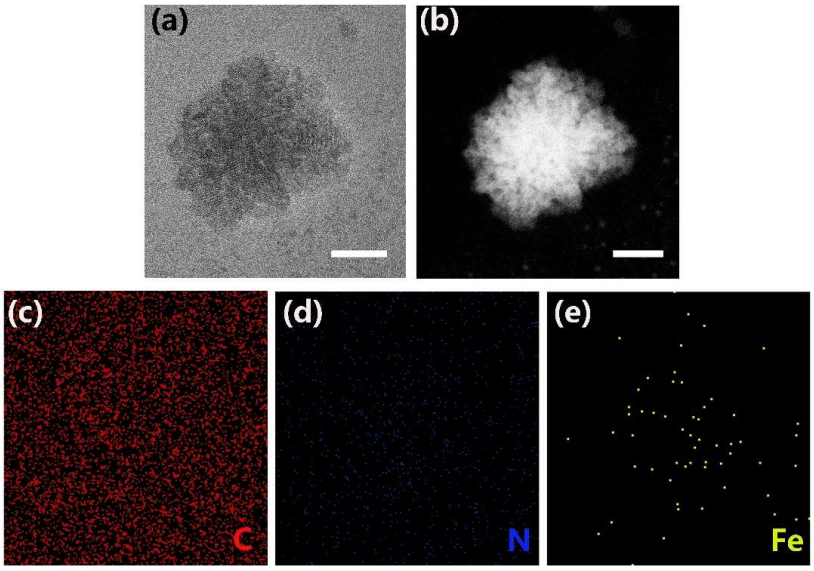

Figure S17. (a) TEM image, (b) HAADF-STEM and (c-e) corresponded EDS-mapping images of N@P-Fe after 5000 CV cycles.

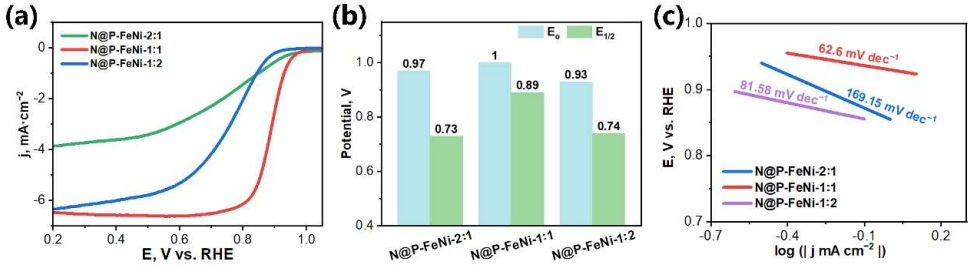

Figure S18. (a) LSV curves of N@P-FeNi-1:2, N@P-FeNi-1:1, N@P-FeNi-2:1 at a rate of 10mV·s^{-1} at 1600 rpm. (b) The comparison of E_o and $E_{1/2}$ of N@P-FeNi-1:2, N@P-FeNi-1:1, N@P-FeNi-2:1. (c) Tafel plots of N@P-FeNi-1:2, N@P-FeNi-1:1, N@P-FeNi-2:1.

Table S11. A comparative summary of key metrics for N@P-FeNi, N@P-Fe and other metal-doped core-shell-derived carbons reported in the literature.

Catalyst	E_0 (V)	$E_{1/2}$ (V)	j_L (mA·cm^{-2})	Reference
N@P-FeNi	1.00	0.89	6.46	This work
N@P-Fe	0.98	0.88	5.67	This work
Fe/Fe_3C@NC	–	0.86	5.57	[31]
FeNC@F127	–	0.87	5.14	[32]
Fe_5C_2@SNC	–	0.86	5.8	[33]
FeNi-NPC-1000	0.89	0.877	3.75	[34]
Co-N-PC	–	0.833	5.70	[35]
Co@C(N)	0.99	0.76	4.99	[36]
NiCo@NpC	0.879	0.78	5.12	[37]
Cu@C(N)	0.95	0.77	5.66	[38]
Co@NC@CNTs	–	0.82	5.40	[39]
Fe_3O_4/N-HCSC	1.024	0.846	5.69	[40]
FFCN-MP4000	0.96	0.83	6.6	[41]
NC@Co-NGC DSNC	0.92	0.82	5.25	[42]

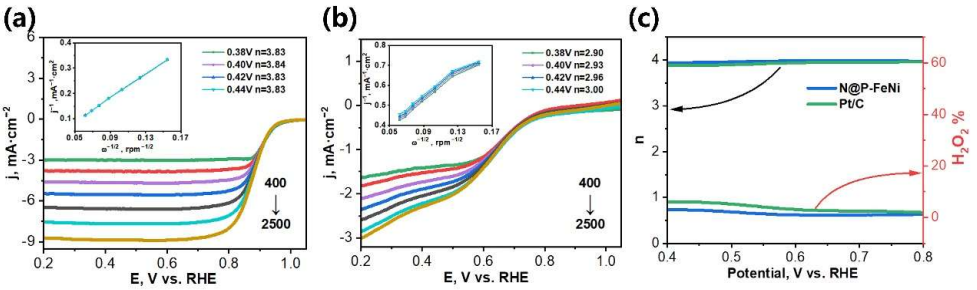

Figure S19. LSV curves of (a) N@P-FeNi and (b) N@P-Ni at a series of rotation speeds from 400 to 2500 rpm and the fitted K-L plots at different potentials. (c) H_2O_2 yield and electron transfer number n from the RRDE test of N@P-FeNi and Pt/C.

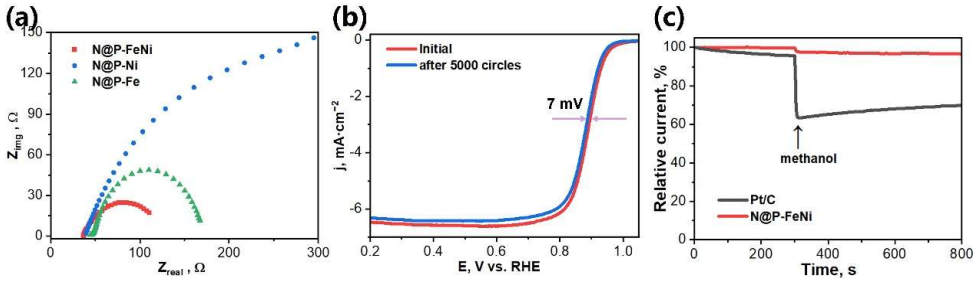

Figure S20. (a) Nyquist plots of N@P-Fe, N@P-Ni, N@P-FeNi. (b) LSV curves of N@P-FeNi before and after 5000 CV cycles. (c) The $i-t$ response curves for the methanol immunity experiments of N@P-FeNi and Pt/C.

Zidan Zhang has been a Master's student in Materials Science at Nanjing University of Science and Technology, China, since 2025. (Email: 125116023965@njust.edu.cn)

Huan Wu received her Master degree in Material Science from Nanjing University of Science and Technology, China, in 2026. (Email: huan@njust.edu.cn)

Boyu Jia has been a Master's student in Materials Science at Nanjing University of Science and Technology, China, since 2024. (Email: 124116023841@njust.edu.cn)

Qingmin Ji received her PhD degree in chemistry from University of Tsukuba, Japan, in 2005. She then worked in National Institute of Advanced Industrial Science and Technology (AIST) and National Institute for Materials Science (NIMS) in Japan before joining Nanjing University of Science and Technology. Her current research focuses on the design of hybrid functional structures by self-assembly and exploring their advanced applications for sensing and catalysis. (Email: jiqingmin@njust.edu.cn)

Hengdao Quan is currently working as a group leader and full Professor at the University of Shanghai for Science and Technology. His research area focuses on fluorine chemistry, catalysis chemistry and organic chemistry. He has successfully developed a new generation of environmentally friendly fluorinated products, including refrigerants, cleaning agents, electronic etching gases, and insulating gases. (Email: quanhengdao@usst.edu.cn)